

2

Thermo-Optic Effects in Polymer Bragg Gratings

Avram Bar-Cohen, Bongtae Han, and Kyoung Joon Kim

University of Maryland, College Park, Maryland, USA

2.1. INTRODUCTION

In spite of their relatively high light absorption rate, polymer materials provide a potent alternative to conventional optical materials due to low-cost, ease of fabrication and assembly, and compatibility with other materials. The recent literature reveals a rapidly increasing interest in the use of polymer components in photonics systems. While polymer waveguides are currently receiving much of the attention, it is to be expected that signal management requirements will lead to progressively greater efforts in gratings, mirrors, and lenses.

A Bragg grating (BG) in a light transmitting waveguide produces a very narrow band of reflected optical energy, with a maximum reflectivity at the characteristic wavelength of the grating, called the *Bragg wavelength*, as illustrated in Figure 2.1. Unlike the conventional glass fibers, the index of refraction in light-transmitting polymers typically varies inversely with the temperature, leading to negative thermo-optic coefficients that are 10 to 30 times greater than the positive thermo-optic coefficient of conventional silica glass [1]. This strong negative thermo-optical characteristic imbues polymer BGs, generally packaged on low thermal expansion substrates, with precise wavelength discrimination when used as tuning filters.

Another important characteristic of polymeric optical materials is their relatively high light absorption rates, at approximately 0.2 dB/cm, as compared to 0.2 dB/km for glass fibers at wavelengths of 1550 nm. However, as shown in Figure 2.2 for the acrylic-based polymers of allied signal [1], the absorption rates of polymeric optical materials strongly depend on the wavelength. For example, in acrylic with full CH content the absorption rate (0.5 dB/cm) at 1.55 μm is 25 times greater than that at 0.8 μm .

Intrinsic self-heating, resulting from these high absorption rates, can produce considerable temperature changes within polymer waveguides and gratings. Such self-heating, as well as the induced temperature gradients and possible changes in the ambient temperature, can cause undesirable shifts in the Bragg wavelength and changes in the reflectivity/transmissivity of the grating. To facilitate the selection of polymeric optical materials

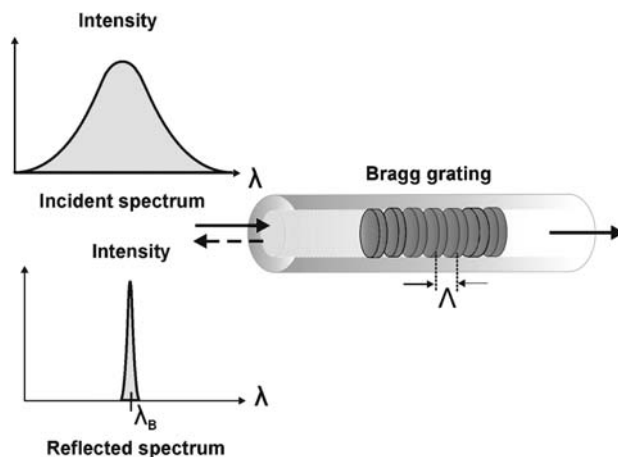


FIGURE 2.1. Fundamental characteristics of Bragg grating.

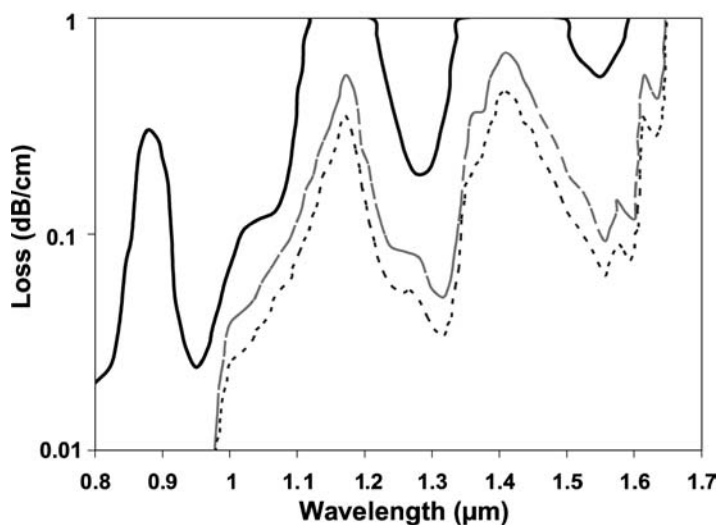


FIGURE 2.2. Light absorption in polymer systems (allied signal acrylic: solid line—100% CH; dashed line—30% CH; dotted line—20% CH) [1].

and the rational design of polymer BGs, a complete understanding of thermo-optic behavior of polymer BGs is required.

This chapter, thus, focuses on the derivation and exploration of a thermo-optical model that can be used to characterize the thermally-induced optical behavior of a polymer fiber Bragg grating (PFBG). The results and implications of an extensive parametric study, using two distinct light sources, are presented and discussed.

2.2. FUNDAMENTALS OF BRAGG GRATINGS

2.2.1. Physical Descriptions

A Bragg grating (BG) can be formed by index modulations in the waveguide material, induced by exposure to ultraviolet (UV) light and/or doping [2–4], or by trenching (interrupting) of the waveguide material with etchants and/or focused laser beams [5]. A BG formed by UV exposure and/or doping, without physical trenches, is referred to as a *bulk index grating*, and a BG formed by physical deformation is referred to as a *surface relief grating*. Bragg gratings (BGs) can be found in numerous photonic components and systems, including distributed feedback laser diodes (DFB LD), distributed Bragg reflector laser diodes (DBR LD), optical fibers, and planar waveguides.

Two most popular forms of BGs are illustrated in Figures 2.3 and 2.4; a fiber Bragg grating (FBG) and a planar Bragg grating (PBG). A FBG is a BG in an optical fiber, and a PBG is a BG in a planar waveguide. A FBG is usually a bulk index grating, while both surface relief and bulk indexing are used to create a PBG.

Figure 2.5 illustrates the most widely used *phase-mask* technique to inscribe a BG in an optical fiber [3], using a diffractive optical component (a transmission diffraction grating) as a phase-mask. The phase mask is especially fabricated to suppress the zeroth order diffraction, while the ± 1 st diffraction orders interfere to produce a sinusoidal intensity distribution in space. A doped photosensitive optical fiber is placed in the region where the two beams intersect and a BG is imprinted on a glass or polymer fiber. Inscription of a BG in a polymer optical fiber requires more rigorous fabrication techniques because of its much higher UV absorption rate [6].

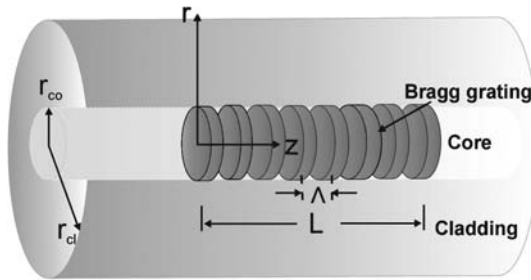


FIGURE 2.3. Fiber Bragg grating structure.

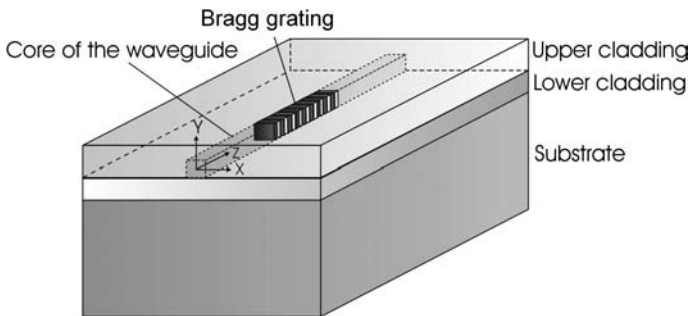


FIGURE 2.4. Packaged planar Bragg grating structure.

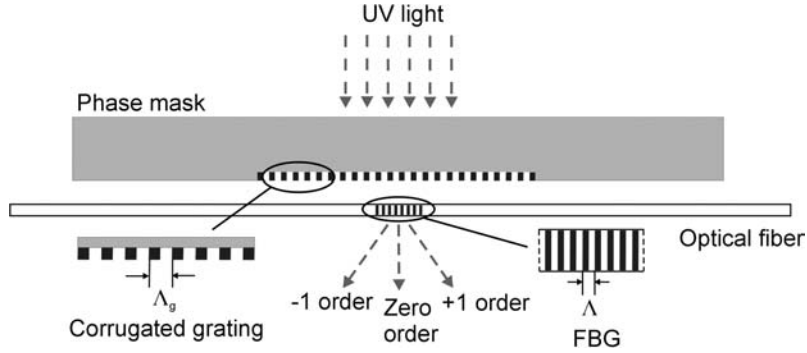


FIGURE 2.5. Phase-mask technique for fiber Bragg grating fabrication.

Since formation of a permanent BG in a glass optical fiber was first demonstrated by Hill et al. [4], BGs integrated fibers and other waveguides have been among the key components in photonic systems. They have been used widely for filtering, switching and stabilizing optical signals in telecommunication applications such as Wavelength Division Multiplexing/Demultiplexing (WDM) and Optical Add-Drop Multiplexing (OADM) [5]. With their simplicity and unique filtering characteristics, BGs have also been used as narrow band reflectors in wavelength stabilized lasers, fiber lasers, and pump amplifiers [2,5]. More recently, FBG sensors have been proposed as future medical sensor systems to measure temperatures during medical treatments [7–11]. A FBG is dielectric, and thus unlike thermocouples and thermistors, or other conventional temperature measuring electronic devices, it is immune to electromagnetic interference.

Polymer BGs have been proposed as passive filters [12–14], tuning filters [15,16], WDM systems [1,17–19] and couplers [20]. A very narrow spectral bandwidth of ~ 0.2 nm at 1550 nm was demonstrated using passive polymer BG filters with uniform grating periods [12], and a even narrower band of 0.03 nm at 1290 nm was demonstrated using phase shifted BG filters [13]. Polymer BGs have also been demonstrated as filters in WDM systems for short haul data transmission with a wavelength tolerance of 0.2 to 0.5 nm/K [1,15]. As a future solution for an economical multiplexing system, polymer BG-based optical add/drop multiplexers (OADM's) were introduced with a channel spacing of 400 GHz (3.2 nm) and a thermal stability of 0.04 nm/K [19].

2.2.2. Basic Optical Principles

The axial refractive index modulation in a BG is typically represented in sinusoidal form [21], as illustrated in Figure 2.6 and expressed in Equation (2.1)

$$\delta n_{eff}(z) = \overline{\delta n_{eff}(z)} \left[1 + \cos \left(\frac{2\pi z}{\Lambda} + \phi(z) \right) \right], \quad (2.1)$$

where $\delta n_{eff}(z)$ is the modulation of the effective refractive index, $\overline{\delta n_{eff}(z)}$ is the average modulation of the effective refractive index, Λ is the grating period, and $\phi(z)$ is a grating chirp, i.e., the inherent or fabricated non-uniformity in the grating period.

As light is incident on the fiber, entering from the left in Figure 2.6, the refractive index modulation results in the reflection of a narrow bandwidth of light, centered around

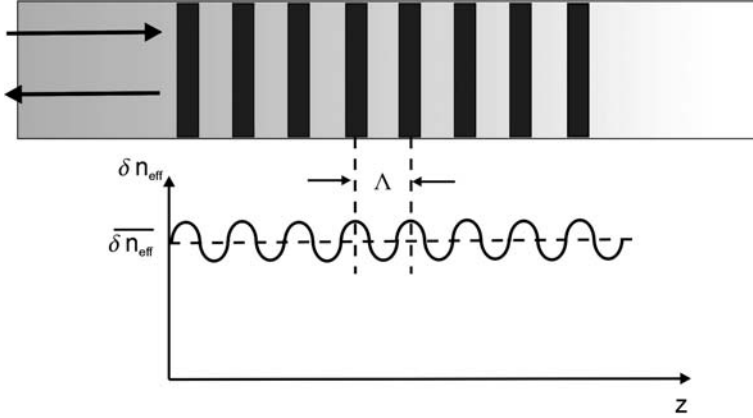


FIGURE 2.6. Refractive index modulation along Bragg grating.

the Bragg wavelength, λ_B . This characteristic wavelength is determined by the effective refractive index and the grating period and can be defined as [21]

$$\lambda_B = 2n_{eff}\Lambda, \quad (2.2)$$

where n_{eff} is the effective refractive index.

The intrinsic optical parameters of FBGs include the refractive indices of the fiber core and the cladding (n_{co} and n_{cl}), the index modulation ($\delta n_{eff}(z)$), and the grating period (Λ). From these intrinsic parameters, working through several defined optical parameters, the effective refractive index (n_{eff}), Bragg wavelength (λ_B), coupling coefficient (κ) (relating to the interaction between the incident and reflected waves in the BG), and maximum reflectivity (ρ_{max}) can be determined.

For single mode operation, the Numerical Aperture, NA is defined [22] as

$$NA = \sin \phi_{max} = \sqrt{n_{co}^2 - n_{cl}^2}, \quad (2.3)$$

where ϕ_{max} is the critical angle (or the maximum incident angle for total internal reflection).

For single mode operation, the generalized frequency, V , defined in Equation (2.4), must be maintained below 2.4048 [22], i.e.,

$$V = \frac{2\pi r_{co}}{\lambda} NA < 2.4048, \quad (2.4)$$

where r_{co} is the core radius.

This leads a relation for the generalized guide index, b , given by Equation (2.5)

$$b = \left(1.1428 - \frac{0.996}{V} \right)^2. \quad (2.5)$$

Reflecting the combined effects of the numerical aperture, guide index, and cladding refractive index, the effective index of refraction, n_{eff} , can be expressed as [22]

$$n_{eff} = \sqrt{b \cdot (NA)^2 + n_{cl}^2}. \quad (2.6)$$

Substituting Equation (2.2) through (2.5) into Equation (2.6) and rearranging the terms, the n_{eff} relation takes the following form

$$\left[1 - \frac{0.996^2}{(\pi r_{co})^2} \Lambda^2\right] n_{eff}^2 + 2.2765 \frac{\Lambda \cdot NA}{\pi r_{co}} n_{eff} - n_{cl}^2 - (1.1428)^2 NA^2 = 0, \quad (2.7)$$

where single mode operation dictates that the solution of Equation (2.7) for the effective index must satisfy the following relationship

$$n_{eff} > \frac{\pi \cdot r_{co} NA}{2.4048 \cdot \Lambda}.$$

Using the intrinsic parameters (r_{co} , n_{co} , n_{cl} , and Λ) of a FBG, the effective index of the FBG can be evaluated using Equation (2.7).

For a single mode BG [23,24], the coupling coefficient, κ is defined as

$$\kappa = \frac{\pi}{\lambda} \overline{\delta n_{eff}}. \quad (2.8)$$

Then, the maximum reflectivity, produced at the Bragg resonance condition, is

$$\rho_{max} = \tanh^2(\kappa_B L), \quad (2.9)$$

where L is the total grating length (Figure 2.3) and κ_B is the coupling coefficient at the Bragg wavelength, λ_B .

2.3. THERMO-OPTICAL MODELING OF POLYMER FIBER BRAGG GRATING

This section presents a methodology for thermo-optical modeling of a polymer fiber Bragg grating (PFBG) associated with the intrinsic absorption of light energy. An analytical formulation based on a modified coupled-mode theory is described, which determines the power variation induced by the coupling between counter-directional light waves within the PFBG. An analytical description for absorption-induced heat generation is provided and a semi-numerical thermo-optical model, using the modified Transfer Matrix Method (TMM), along with a simple analytical thermo-optical model, is also given.

2.3.1. Heat Generation by Intrinsic Absorption

2.3.1.1. Power Spectra of Light Sources The radial variation of the power irradiance, $I(r)$, of a light source, can be assumed to follow a Gaussian profile, and to be given by [22]

$$I(r) = \frac{2P_{inc}}{\pi w^2} e^{-2r^2/w^2}, \quad (2.10)$$

where P_{inc} is the incident optical power and w is the beam radius. The beam radius, w , can be defined as [25]

$$w = \sqrt{\frac{-2r_{co}^2}{\ln(1 - \Gamma)}}, \quad (2.11)$$

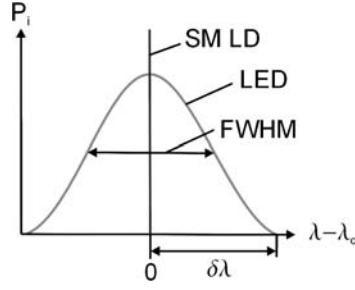


FIGURE 2.7. Power spectra of Light Emitting Diode and Single Mode Laser Diode.

where r_{co} is the radius of the core of the fiber and Γ is the power confinement factor; which determines the fraction of the incident optical power which actually enters the core of the fiber. In this study, the power confinement factor, Γ , is defined as [25]

$$\Gamma = \frac{P_{co}}{P_{tot}}, \quad (2.12)$$

where P_{co} is the power in the core, and P_{tot} is the total power illuminating the fiber. The confinement factor [25] is governed by various optical parameters. Using a Bessel function formulation, the confinement factor is found to be [25]

$$\Gamma = b \left[1 - \frac{J_0^2(V\sqrt{1-b})}{J_1(V\sqrt{1-b})J_{-1}(V\sqrt{1-b})} \right], \quad (2.13)$$

where V and b are the previously defined generalized frequency [see Equation (2.4)] and generalized guide index [see Equation (2.5)] of the fiber.

Engineering data [26,27] for typical light sources of interest suggests that the power spectra of both Single Mode Laser Diodes (SM LD's) and Light Emitting Diodes (LED's) often follow a Gaussian distribution. The normalized spectral power density, $\overline{P}(\lambda)$, for these light sources can, thus, be expressed as

$$\overline{P}(\lambda) = B e^{4 \ln 0.5 ((\lambda - \lambda_c)/FWHM)^2}, \quad (2.14)$$

$$B = \frac{1}{2 \int_0^{\delta\lambda} e^{4 \ln 0.5 ((\lambda - \lambda_c)/FWHM)^2} d(\lambda)},$$

where $\delta\lambda$ is half of the total spectral bandwidth and FWHM is the “full width half maximum,” which defines the spectral bandwidth at half of the maximum power. The central wavelength of the light source is given by λ_c . Figure 2.7 illustrates the power spectra of a typical LED and a SM LD.

2.3.1.2. Power Variation Along a PFBG The optical characteristics of the BG, including the reflection spectrum and the reflectivity, can be explained well by the coupled-mode theory [28–30]. Wave propagation in the BG can be described by the scalar wave equation [28] as

$$\frac{\partial^2 E}{\partial z^2} + k_c^2 E = 0, \quad (2.15)$$

where E is the complex amplitude of the electrical field and k_c is the wave number in a lossy medium [28], as follows

$$k_c^2 = \beta^2 - i \cdot \hat{a}\beta + 4\kappa\beta \cos(2\beta_B z), \quad (2.16)$$

where the propagation constant β [28] is defined as

$$\beta = \frac{2\pi n_{eff}}{\lambda}. \quad (2.17)$$

In Equation (2.16), β_B is the propagation constant at the Bragg condition, \hat{a} is the intrinsic absorption coefficient, and κ is the coupling coefficient. It is to be noted that the absorption coefficient, \hat{a} (m^{-1}), used in the present analysis is related to the more common dB-based absorption coefficient, a (dB/cm) by

$$\hat{a} = 10 \cdot a \ln(10). \quad (2.18)$$

For example, an absorption coefficient of 11.513 m^{-1} is equal to 0.5 dB/cm, and is represents about 10% of optical power loss along 1 cm of propagation.

Following the approach proposed by Kogelnik [28], the electrical field in a FBG can be written as

$$E(z) = R(z)e^{-i\beta_B z} + S(z)e^{i\beta_B z}, \quad (2.19)$$

where $R(z)$ and $S(z)$ are the amplitudes of the forward traveling and backward traveling waves, respectively. Substituting Equations (2.16), (2.17) and (2.19) into (2.15), we obtain

$$\begin{aligned} \frac{\partial^2 E}{\partial z^2} + k_c^2 E = & e^{-i\beta_B z} R'' - (2i\beta_B e^{-i\beta_B z}) R' - R[e^{-i\beta_B z}(-\beta^2 + i \cdot \hat{a}\beta + \beta_B^2) \\ & - 2\kappa\beta(e^{i\beta_B z} + e^{-i \cdot 3\beta_B z})] + e^{i\beta_B z} S'' + (2i\beta_B e^{i\beta_B z}) S' \\ & + S[e^{i\beta_B z}(-\beta^2 - i \cdot \hat{a}\beta + \beta_B^2) + 2\kappa\beta(e^{-i\beta_B z} + e^{i \cdot 3\beta_B z})] = 0. \end{aligned} \quad (2.20)$$

Assuming the amplitudes (R and S) vary slowly, R'' and S'' can be neglected in Equation (2.20) [28]. Furthermore, as can be seen in Equation (2.17), β is extremely large, and thus oscillating terms with much higher frequency than the Bragg frequency, i.e., $e^{i \cdot 3\beta_B z}$ and $e^{-i \cdot 3\beta_B z}$ can be also neglected [28]. Equation (2.20) can then be rewritten as

$$\begin{aligned} & -(2i\beta_B e^{-i\beta_B z}) R' - R[e^{-i\beta_B z}(-\beta^2 + i \cdot \hat{a}\beta + \beta_B^2) - 2\kappa\beta e^{i\beta_B z}] \\ & + (2i\beta_B e^{i\beta_B z}) S' + S[e^{i\beta_B z}(-\beta^2 - i \cdot \hat{a}\beta + \beta_B^2) + 2\kappa\beta e^{-i\beta_B z}] = 0. \end{aligned} \quad (2.21)$$

Comparing terms with equal exponentials in Equation (2.21), the following coupled differential equations are obtained

$$\begin{aligned} \frac{dR}{dz} = & -\left(\frac{\beta}{\beta_B} \frac{\hat{a}}{2} - \frac{\beta^2 - \beta_B^2}{i \cdot 2\beta_B}\right) R + \frac{\beta}{i\beta_B} \kappa S, \\ \frac{dS}{dz} = & \left(\frac{\beta}{\beta_B} \frac{\hat{a}}{2} - \frac{\beta^2 - \beta_B^2}{i \cdot 2\beta_B}\right) S - \frac{\beta}{i\beta_B} \kappa R. \end{aligned} \quad (2.22)$$

Assuming departures from Bragg wavelength are very small, i.e., $(\beta^2 - \beta_B^2)/(2\beta_B) \approx \beta - \beta_B$ and $\beta/\beta_B \approx 1$, Equation (2.22) can be rewritten as the following coupled differential equations, which are frequently referred to as the “*coupled-mode*” equations, [21,28]

$$\begin{aligned}\frac{dR}{dz} &= -\left(\frac{\hat{a}}{2} + i\delta\right)R(z) - i\kappa S(z), \\ \frac{dS}{dz} &= \left(\frac{\hat{a}}{2} + i\delta\right)S(z) + i\kappa R(z),\end{aligned}\quad (2.23)$$

where δ is the detuning value, which represents the departure of the propagation constant from the Bragg resonance and it is defined as [21]

$$\delta = \beta - \beta_B = \frac{2\pi n_{eff}}{\lambda} - \frac{\pi}{\Lambda}. \quad (2.24)$$

The detuning parameter, δ , is a measure of the spectral proximity of the incident light to the Bragg wavelength. For small values of δ much of the incident light will be reflected by the BG, creating a backward moving wave and transferring a significant amount of energy into the reflected wave, while for large detuning values nearly all the incident light will pass through the waveguide with little energy exchange between the counter directional waves.

The closed form solutions of the coupled-mode equations can be written as

$$\begin{aligned}R(z) &= r_1 e^{mz} + r_2 e^{-mz}, \\ S(z) &= s_1 e^{mz} + s_2 e^{-mz},\end{aligned}\quad (2.25)$$

where the Eigen value of the coupled-mode equations is

$$m = \sqrt{\left(\frac{\hat{a}}{2} + i\delta\right)^2 + \kappa^2}. \quad (2.26)$$

In solving these equations use is made of the boundary conditions, which set the amplitude of the forward wave at the inlet to unity and the amplitude of the backward moving wave at the outlet to zero ($R(0) = 1$ and $S(L) = 0$). A detailed mathematical procedure to obtain the four coefficients in Equation (2.25), using the above boundary conditions, is shown in Appendix A.

Using the DeMoivre’s formula [31], the Eigen value can be expressed as a complex variable, i.e.,

$$m = m_1 + im_2, \quad (2.27)$$

where m_1 and m_2 are real numbers defined as

$$m_1 = \sqrt{\frac{1}{2} \left\{ \sqrt{\left[\left(\frac{\hat{a}}{2}\right)^2 - \delta^2 + \kappa^2 \right]^2 + (\hat{a}\delta)^2} + \left[\left(\frac{\hat{a}}{2}\right)^2 - \delta^2 + \kappa^2 \right] \right\}}, \quad (2.28)$$

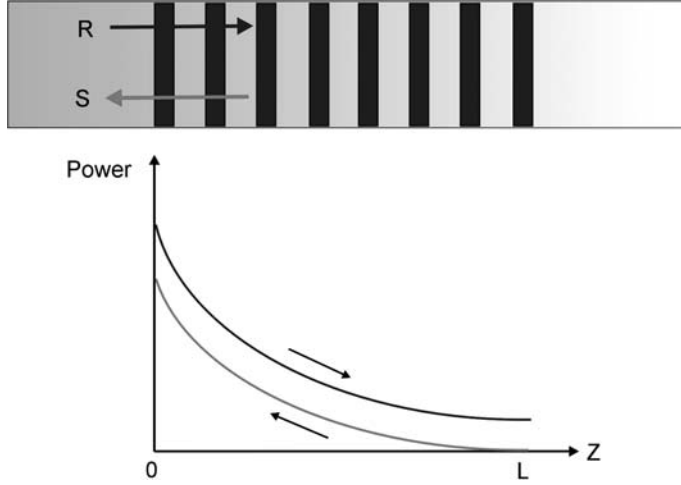


FIGURE 2.8. Axial power variations of incident and reflected light waves in Bragg grating.

$$m_2 = \sqrt{\frac{1}{2} \left\{ \sqrt{\left[\left(\frac{\hat{a}}{2} \right)^2 - \delta^2 + \kappa^2 \right]^2 + (\hat{a}\delta)^2} - \left[\left(\frac{\hat{a}}{2} \right)^2 - \delta^2 + \kappa^2 \right] \right\}}. \quad (2.29)$$

Substituting Equation (2.27) into Equation (2.25), the amplitudes of the two waves (i.e., general solutions of the coupled-mode equations) can be rewritten as

$$R = 2r_1 e^{m_2 z} [\sinh(m_1 z)] + e^{-m_1 z} (r_1 e^{im_2 z} - r_1 e^{-im_2 z} + e^{-im_2 z}), \quad (2.30)$$

$$S = 2(e^{im_2 z} s_1 e^{m_1 L}) \sinh[m_1(z-L)] + s_1 e^{-m_1 z} (e^{im_2 z} - e^{im_2(2L-z)}) e^{2m_1 L}. \quad (2.31)$$

By multiplying the conjugates of the complex amplitudes of two waves, the axial power of the forward and backward moving waves, respectively, can be expressed as

$$|R|^2 = \frac{c_1 e^{2m_1 z} + c_2 e^{2m_1(2L-z)} + c_3 \cos[2m_2(z-L)] + c_4 \sin[2m_2(z-L)]}{c_1 + c_5 + c_2 e^{4m_1 L}}, \quad (2.32)$$

$$|S|^2 = \frac{c_6 \{e^{2m_1 z} + e^{2m_1(2L-z)} - 2e^{m_1 L} \cos[2m_2(z-L)]\}}{c_2 \kappa^2 e^{4m_1 L} + c_1 \kappa^2 + c_7}. \quad (2.33)$$

The complete mathematical descriptions of the coefficients can be also found in Appendix A.

Figure 2.8 illustrates the power variations of forward and backward traveling waves propagating through a PFBG at the Bragg condition. The exponentially decaying power of the forward moving wave is mainly due to the strong coupling (or transfer) to the backward moving light wave and results in the exponentially increasing power of the reflected wave, traversing the waveguide in the opposite direction.

However, the coupled-mode equations [Equation (2.23)]—in either numerical or closed form—can not be used to determine the power variations through the BG for wavelengths that depart even modestly from the Bragg resonance. This limitation of the coupled-mode equations is mainly due to the fundamental assumptions; i.e., small departures from

Bragg resonance and negligible second derivatives of the wave amplitudes; these assumptions were used for the “coupled mode equation” solution obtained by Kogelnik [28] and the present study follows his approach.

Although the literature does not appear to contain analyses that remove either of these limitations, it is possible to obtain an approximate solution of the coupled mode equations by recognizing and exploiting physical characteristics of the forward and backward moving waves in the BGs at wavelengths that are somewhat removed from the Bragg wavelength, but still within the bandwidth of the grating. Due to the energy transfer between the two light waves, the power of both the incident and reflected waves must decrease along the axis of the BG. Therefore, the local axial gradients of the optical power of the two waves can be assumed to be negative, i.e.,

$$\frac{d(|R|^2)}{dz} < 0 \quad \text{and} \quad \frac{d(|S|^2)}{dz} < 0. \quad (2.34)$$

In addition, the fundamental assumption underpinning the coupled-mode equations, i.e., slowly varying amplitudes of the two waves, suggests that the local gradients of the optical powers vary smoothly along the grating. This implies that the second derivatives of the optical powers should be small, i.e.,

$$\frac{d^2\{|R|^2\}}{dz^2} \approx 0 \quad \text{and} \quad \frac{d^2\{|S|^2\}}{dz^2} \approx 0. \quad (2.35)$$

Modifying Equations (2.32) and (2.33) to satisfy the conditions of Equations (2.34) and (2.35) and applying the previously stated power boundary conditions at the inlet and outlet of the grating, it is possible to estimate the axial variation in the forward moving and backward moving wave as

$$|R|^2 = \frac{c_1 e^{2m_1 z} + c_2 e^{2m_1(2L-z)} + c_3 \left[\frac{(1 - \cos 2m_2 L)}{L} z + \cos 2m_2 L \right] + c_4 \left[\frac{(\sin 2m_2 L)}{L} z - \sin 2m_2 L \right]}{c_1 + c_5 + c_2 e^{4m_1 L}}, \quad (2.36)$$

$$|S|^2 = \frac{c_6 \left\{ e^{2m_1 z} + e^{2m_1(2L-z)} - 2e^{2Lm_1} \left[\frac{(1 - \cos 2m_2 L)}{L} z + \cos 2m_2 L \right] \right\}}{c_2 \kappa^2 e^{4m_1 L} + c_1 \kappa^2 + c_7}. \quad (2.37)$$

For light wavelengths sufficiently removed from λ_B , the BG reverts to a simple waveguide, producing no backward moving wave and no reflection. Under these circumstances, the axial power variation of the wave incident on the grating approaches that associated with Beer’s law. Consequently, the power of the forward moving wave at the end of the grating can be expressed as

$$|R|^2|_{z=L} \approx e^{-\hat{a}L}. \quad (2.38)$$

By setting the value of $|R|^2$ from Equation (2.36) to that given by Equation (2.38), simple criteria for determining the bandwidth of the grating can be obtained. For wavelengths greater (and smaller) than the λ needed to match these two values, Beer’s law can be em-

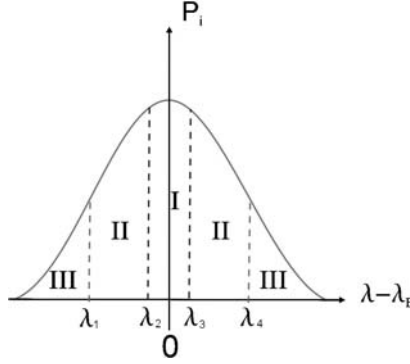


FIGURE 2.9. Light propagation zones in Bragg grating.

ployed to describe the optical power variations through the grating. In this region, the optical power of the two waves becomes

$$|R|^2 = e^{-\hat{a}z}, \quad (2.39)$$

$$|S|^2 = 0. \quad (2.40)$$

Figure 2.9 illustrates the three zones of power variations along BGs: a central zone at and close to the Bragg wavelength (I)—given by the solutions of the coupled-mode equations [Equations (2.32) and (2.33)] the grating bandwidth zone (II)—given approximately by the modified solutions of the coupled-mode equations [Equations (2.36) and (2.37)] and a third zone in which the grating behaves simply as a waveguide (III)—for which Beer’s law [Equations (2.39) and (2.40)] can be used. It should be noted that the existence of these three zones in any particular application depends on the bandwidth of the light source; while a broad-band LED centered on λ_B could be expected to give rise to all three zones of behavior, a typical narrow-band SM LD may operate entirely in the domain of the coupled-mode equations (central zone I).

To illustrate the above criteria and thus to concretize the spectral behavior of a PFBG, it is instructive to consider a specific case, for which λ_B is equal to 1550 nm, and κ and \hat{a} are 144.4 m^{-1} and 11.5 m^{-1} , respectively. The axial power of the forward moving wave was calculated using Equations (2.32) and (2.33) and the results are shown in Figure 2.10. It is clear from Figure 2.10 that, for values of detuning greater than $0.23 \times 10^{-6} \text{ nm}^{-1}$, the axial gradient becomes positive and the power of the forward moving wave exceeds unity. Taking n_{eff} of 1.5, Equation (2.24) can be used to convert this “bounding” detuning value to a limiting wavelength of 0.06 nm, which defines the transition from Zone I to Zone II.

The grating bandwidth—obtained by allowing $|R|^2$ from Equation (2.36) to approach within 1% of the value given by Beer’s law [Equation (2.38)]—can be numerically found and it lies in the range of $|\delta| < 2.3 \times 10^{-6} \text{ nm}^{-1}$. The corresponding wavelength range is $|\lambda - \lambda_B| < 0.6 \text{ nm}$. Beyond this range, light propagates without interference from the BG and this range defines the outer boundary of Zone II.

2.3.1.3. Heat Generation in a PFBG The distribution of the optical power, $P(\lambda, r, z)$, can be expressed as

$$P(\lambda, r, z) = I(r) \overline{P(\lambda)} [|R(\lambda, z)|^2 + |S(\lambda, z)|^2]. \quad (2.41)$$

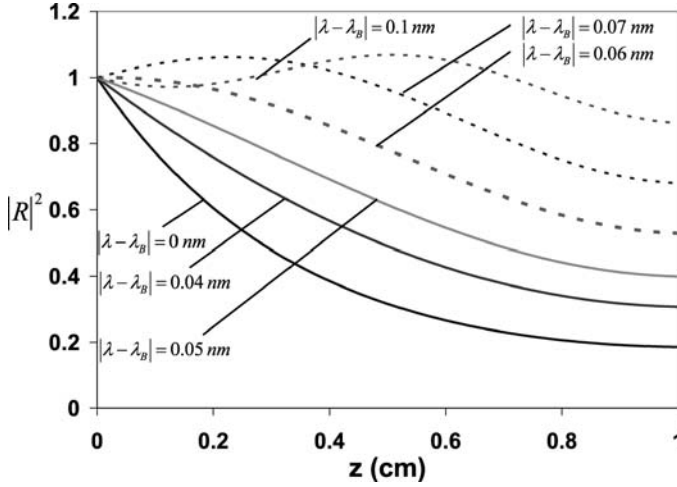


FIGURE 2.10. Axial power variation of incident light in typical polymer fiber Bragg grating.

Accordingly, heat generation at each wavelength, induced by the intrinsic absorption of light energy, can be expressed as

$$q_G(\lambda, r, z) = P(\lambda, r, z) \cdot \hat{a}(\lambda, r, z) \cong P(\lambda, r, z) \cdot \hat{a}, \quad (2.42)$$

where the absorption coefficient is assumed to be constant along the length of the grating and across the wavelength range of interest. Heat generation produced by the full spectrum of incident light can be obtained by integrating the spectral heat generation over the three zones of grating behavior, spanning the full spectral bandwidth, as

$$\begin{aligned} q_G(r, z) &= \left[\int_I q_G(\lambda, r, z) d\lambda + \int_{II} q_G(\lambda, r, z) d\lambda + \int_{III} q_G(\lambda, r, z) d\lambda \right] \\ &= \hat{a} \cdot \left\{ \int_I I(r) \overline{P(\lambda)} [|R(\lambda, z)|^2 + |S(\lambda, z)|^2] d\lambda + \int_{II} I(r) \overline{P(\lambda)} [|R(\lambda, z)|^2 \right. \\ &\quad \left. + |S(\lambda, z)|^2] d\lambda + [I(r) e^{-\hat{a}z}]_{III} \right\}. \end{aligned} \quad (2.43)$$

It is to be noted again that the modified solution [Equations (2.36) and (2.37)] of the coupled-mode equations should be used to determine $|R(\lambda, z)|^2 + |S(\lambda, z)|^2$ for zone II.

A broadband light source, such as an LED with a central wavelength of 1550 nm, typically displays 50–100 nm of FWHM [27], some 50–100 times larger than the grating bandwidth of the specific case considered in the previous section; i.e., Zone III is much greater than Zones I and II. Consequently, the contribution of the reflected (or backward moving) wave is very small and heat generation in a PFBG is primarily associated with absorption across the full bandwidth of the source, and can be expressed in a simple form as

$$q_G(r, z)|_{LED} = I(r) e^{-\hat{a}z} \cdot \hat{a}. \quad (2.44)$$

A typical SM LD has a narrow spectral bandwidth, which is almost always less than 0.3 nm [26]. Thus, for the specific case cited above, the spectrum of such a SM LD would be wholly or substantially contained within the grating bandwidth of the BG. Consequently, much of the light energy entering a PFBG in the forward moving wave will be transferred to the backward moving wave, leading to strong and spectrally complex axial variations in the propagating waves. Determination of the spatial variation of heat generation in a PFBG, under these circumstances, requires a full integration of the intensity relation [Equation (2.42)], repeated here

$$q_G(r, z)|_{SMLD} = \hat{a} \cdot \int P(\lambda, r, z) d\lambda \quad (2.45)$$

2.3.2. Analytical Thermal Model of PFBG

A schematic of the domain and symbols used for the analytical thermal model are shown in Figure 2.11, where r_{cl} is the radius of the entire fiber including its cladding, and r_o is the radius of the volume which contains the total incident optical power. Determination of the steady-state temperature field in the intrinsically-heated PFBG requires a solution of the heat conduction equation with non-uniform heat generation. In cylindrical coordinates, the governing equation for the temperature field can be expressed as [32]

$$\frac{\partial^2 \theta}{\partial r^2} + \frac{1}{r} \frac{\partial \theta}{\partial r} + \frac{\partial^2 \theta}{\partial z^2} + \frac{1}{k} q_G(r, z) = 0, \quad (2.46)$$

where θ is the excess temperature above ambient, and k is the thermal conductivity. The BG axial dimension is much larger than its core diameter, with a typical aspect ratio greater than 100:1. It is thus reasonable to assume uniform heat generation in the radial direction and reduce the above equation to a one-dimensional heat conduction equation.

Inserting the relation for the internal heat generation [Equation (2.44)] for the broad-band LED light source, the one-dimensional heat conduction equation takes the form of

$$\frac{d^2 \theta}{dz^2} - p^2 \theta = \frac{-P_{inc}}{k\pi r_o^2} \cdot e^{-\hat{a}z} \cdot \hat{a}, \quad (2.47)$$

where $p = \sqrt{\frac{2h}{kr_o}}$.

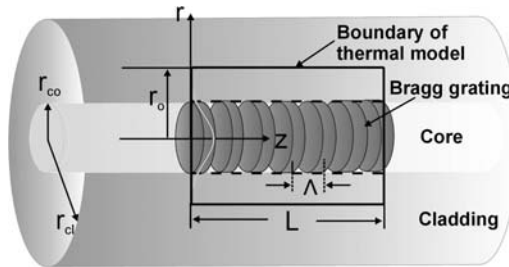


FIGURE 2.11. Geometry of polymer fiber Bragg grating thermal model.

In the above equation, h is the effective heat transfer coefficient on the outer surface of the modeled volume, reflecting the resistance to heat flow through the cladding and then into the ambient, which can be expressed as

$$h = \frac{1}{\frac{r_o}{k} \ln \frac{r_{cl}}{r_o} + \frac{r_o}{h_{cl} r_{cl}}} \cong \frac{r_{cl}}{r_o} h_{cl}, \quad (2.48)$$

where h_{cl} is the total combined (convection and radiation) heat transfer coefficient at the optical fiber surface. For the dimensions and conductivity of typical polymer optical fibers, the conductive term ($r_o/k \cdot \ln(r_{cl}/r_o)$) can be neglected relative to the convective term ($r_o/(h_{cl} r_{cl})$) in the denominator of Equation (2.48), yielding the approximation shown. For example, when r_o , r_{cl} , and k are 7 μm , 50 μm , and 0.2 W/m K, $r_o/(h_{cl} r_{cl})$ ($= 14 \times 10^{-3}$) is about two orders of magnitude greater than $r_o/k \cdot \ln(r_{cl}/r_o)$ ($= 7 \times 10^{-5}$). For purposes of this analysis, the outer surface of the fiber was assumed to be passively cooled by natural convection and radiation, with an approximate heat transfer coefficient of 10 W/m² K.

The general solution of Equation (2.47) can be written as

$$\theta = g_1 e^{pz} + g_2 e^{-pz} + \theta_s. \quad (2.49)$$

The particular solution can be expected to take the form of

$$\theta_s = D e^{-\hat{a}z}. \quad (2.50)$$

The procedure used to solve this equation and the derivation of the particular solution are presented in Appendix B.1. The solution is based on the assumptions that all heat loss occurs from the surface of the fiber, and that heat loss at the fiber BG ends can be neglected, i.e., assuming that both ends of the PFBG are adiabatic, i.e.,

$$\left. \frac{d\theta}{dz} \right|_{z=0} = 0 \quad \text{and} \quad \left. \frac{d\theta}{dz} \right|_{z=L} = 0. \quad (2.51)$$

The heat conduction model associated with a moderately narrow-band SM LD, for which light propagation is expected to occur primarily within zone I and II (ruled by the coupled mode equations) requires use of the more complex internal heat generation relation [Equation (2.45)], i.e.,

$$\frac{d^2\theta}{dz^2} - p^2\theta + \frac{1}{k} \cdot \frac{P_{inc}}{\pi r_o^2} \cdot \int_{\lambda_1}^{\lambda_4} \overline{P(\lambda)} [|R(\lambda, z)|^2 + |S(\lambda, z)|^2] d\lambda \cdot \hat{a} = 0. \quad (2.52)$$

Applying the convective boundary condition on the surface of the fiber, the general solution of Equation (2.52) can be expressed as

$$\theta = d_1 e^{pz} + d_2 e^{-pz} + \theta_p, \quad (2.53)$$

where θ_p is a particular solution for the above conduction equation. The particular solution follows as

$$\theta_p = \int_{\lambda_1}^{\lambda_4} F(\lambda) e^{2m_1(\lambda)z} d\lambda + \int_{\lambda_1}^{\lambda_4} G(\lambda) e^{-2m_1(\lambda)z} d\lambda + \int_{\lambda_2}^{\lambda_3} H(\lambda) \cos[M(\lambda)(z - L)] d\lambda$$

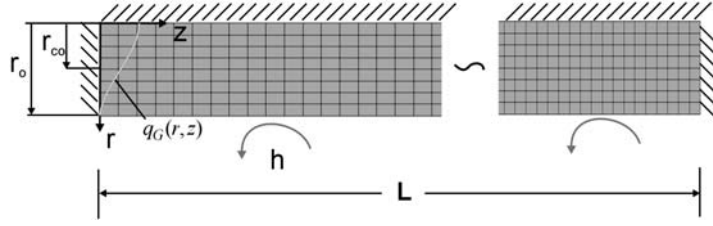


FIGURE 2.12. Geometry of finite element model for polymer fiber Bragg grating.

$$\begin{aligned}
& + \int_{\lambda_2}^{\lambda_3} N(\lambda) \sin[U(\lambda)(z - L)] d\lambda + \int_{\lambda_1}^{\lambda_2} V(\lambda)z + W(\lambda) d\lambda \\
& + \int_{\lambda_3}^{\lambda_4} V(\lambda)z + W(\lambda) d\lambda + \int_{\lambda_1}^{\lambda_2} X(\lambda)z + Y(\lambda) d\lambda \\
& + \int_{\lambda_3}^{\lambda_4} X(\lambda)z + Y(\lambda) d\lambda.
\end{aligned} \tag{2.54}$$

It should be noted that the above particular solution is for a SMLD, whose spectral window ($\lambda_1 \leq \lambda \leq \lambda_4$) lies within zones I and II. More specifically, $\lambda_2 \leq \lambda \leq \lambda_3$ defines zone I, where the closed-form solution of the power variations [Equations (2.32) and (2.33)] should be used. However, in the spectral window, $\lambda_1 \leq \lambda < \lambda_2$ or $\lambda_3 < \lambda \leq \lambda_4$, which lies within zone II, the modified solutions of the power variations [Equations (2.36) and (2.37)] should be employed. Appendix B.2 shows a detailed procedure to obtain the two coefficients (d_1 and d_2) for the general solution, using the above boundary conditions [see Equation (2.51)] as well as the particular solution.

2.3.3. FEA Thermal Model of PFBG

The foregoing analytical thermal model served to capture the salient features of the absorption-induced temperature profile in the polymer fiber BG, but neglected any radial temperature variations that might develop. A Finite Element thermal analysis was conducted to address this issue. Figure 2.12 shows a segment of the solution domain for the two-dimensional axi-symmetric finite-element model. The dimensions and the boundary conditions are the same as those used in the analytical model. The model had approximately 40,000 elements and the volumetric heat sources, $q_G(r, z)$, induced by light absorption in the grating, were applied to the model. In recognition of the high aspect ratio of the fiber and in order to simplify the model, the small heat losses from the ends of the PFBG were ignored, and these surfaces were considered as adiabatic. The numerical simulation was conducted with the PCG solver of ANSYS 8.0 [33].

2.3.4. Thermo-Optical Model of PFBG

Thermally-induced changes of the index and the grating period in the PFBG induce a shift in the Bragg wavelength of the grating. For an isotropic PFBG with a small uni-

form temperature change, these individual effects can be superimposed to yield the Bragg wavelength shift [34]

$$\frac{\Delta\lambda_B}{\lambda_B} = \frac{\Delta n_{eff}}{n_{eff}} + \frac{\Delta\Lambda}{\Lambda}, \quad (2.55)$$

where $\Delta n_{eff}/n_{eff}$ represents the change in the index of refraction resulting from a change in temperature and $\Delta\Lambda/\Lambda$ the contribution of thermal expansion.

By similarity to a glass optical fiber, it can be expected that—despite the small differences in the index of refraction—the core and cladding would be similar in other optical properties. Consequently, the derivative of the effective index of a PFBG with respect to temperature can be taken equal to the dn/dT of the fiber core material and the change in the effective index of refraction be expressed as

$$\Delta n_{eff} = \frac{dn}{dT} \Delta T, \quad (2.56)$$

where dn/dT is the thermo-optical coefficient, and ΔT is the temperature change of the PFBG relative to an appropriate reference temperature. Typical values for dn/dT for glassy polymers range from -100 to $-200 \times 10^{-6}/\text{K}$ [35].

The relative change of the grating period due to thermal expansion is given as

$$\frac{\Delta\Lambda}{\Lambda} = \alpha \Delta T. \quad (2.57)$$

For typical optical polymer materials, the thermal expansion coefficient can be expected to range from 60 to $80 \times 10^{-6}/\text{K}$ [35]. It may, thus, be seen that for polymer optical fibers, the thermo-optic effect and the grating period effect on the Bragg wavelength shift are relatively large and of the same order of magnitude, but opposite in sign. Since the net Bragg wavelength shift is, thus, the difference of two relatively large numbers, care must be taken in evaluating each of the two terms appearing in Equation (2.55). Furthermore, the large magnitude of these terms, as well as the complex and generally non-uniform temperature field induced by the variations in the optical power in the grating close to the Bragg wavelengths, may necessitate use of a more exact relation for $\Delta\lambda_B/\lambda_B$ than offered by the approximate, linear superposition implicit in Equation (2.55). Succeeding paragraphs will provide more rigorous thermo-optical models for the effect of the temperature field on the optical characteristics of a PFBG.

Dealing first with the potentially large magnitude of the Bragg wavelength shift, it is appropriate to return to Equation (2.2) and observe that the shifted Bragg wavelength, λ_{B2} , can be written as

$$\lambda_{B2} = \lambda_{B1} + \Delta\lambda_B = 2(n_{eff1} + \Delta n_{eff})(\Lambda_1 + \Delta\Lambda), \quad (2.58)$$

where subscript “1” denotes the initial state before the temperature change.

Substituting Equations (2.56) and (2.57) into (2.58), one can get

$$\lambda_{B2} = 2 \left(n_{eff1} + \frac{dn}{dT} \Delta T \right) (\Lambda_1 + \Lambda_1 \alpha \Delta T). \quad (2.59)$$

Subtracting the expression for λ_{B1} , the analytical relation for the normalized Bragg wavelength shift, $\Delta\lambda_B$, can be expressed as

$$\frac{\Delta\lambda_B}{\lambda_{B1}} = \left(\frac{1}{n_{eff1}} \frac{dn}{dT} + \alpha \right) \Delta T + \left(\frac{1}{n_{eff1}} \frac{dn}{dT} \cdot \alpha \right) \Delta T^2, \quad (2.60)$$

where $\Delta\lambda_B = \lambda_{B2} - \lambda_{B1}$. It is to be noted that Equation (2.60) provides a more precise relation for the normalized Bragg wavelength shift than offered by Equation (2.55), adding a quadratic dependence on the temperature change to the earlier described linear term. Due to the relatively large thermal expansion coefficient, α , of the PFBG and the relatively small difference between the negative thermo-optic effect and positive grating period effect in the linear ΔT term, this quadratic term can not generally be neglected in the analysis of PFBG. Alternatively, for a glass FBG, the second term in Equation (2.60),

$$\left(\frac{1}{n_{eff1}} \frac{dn}{dT} \cdot \alpha \right) \Delta T^2$$

can be ignored because the product of $1/n_{eff1} \cdot dn/dT$ (6.7×10^{-6}) and α (0.55×10^{-6}) is six orders of magnitude smaller than their sum. For this reason, the thermo-optical dependence of the Bragg wavelength shift of a PFBG is far more complex than that of a glass FBG, which is generally found to vary linearly with temperature.

Several methods for determining the optical field in a non-uniform BG can be found in the literatures [21,36–38]. They include the Transfer Matrix Method (TMM) [21,36,37], direct numerical method [21], and Rouard Method [38]. These methods were developed originally to analyze mechanically chirped gratings, in which the grating period varies along the optical path. However, under the influence of non-uniform light absorption, and the consequent non-uniform heating, a uniform grating period may become “chirped,” thus making these classical approaches suitable for the thermo-optic analysis of a PFBG. Of the choices available, the Transfer Matrix Method was chosen for implementation since it is relatively simple but appears to offer the desired accuracy.

The Transfer Matrix Method employs an analytical matrix solution to relate any two pairs of intensities (e.g., incident and reflected at the entrance) to any other two intensities (e.g., the transmitted and entering at the outlet), and is most often used to determine the reflectivity of a specified BG. As illustrated in Figure 2.13, the optical characteristics of

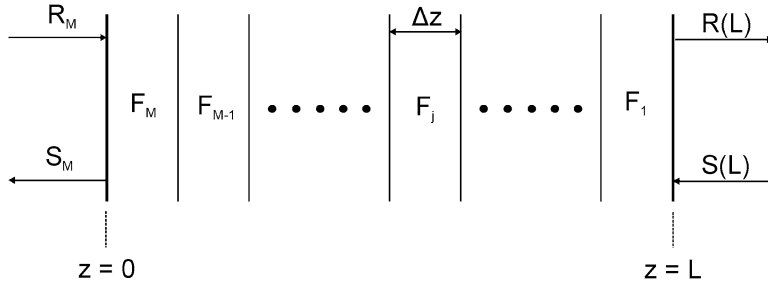


FIGURE 2.13. Illustration of Transfer Matrix Method (TMM).

each small segment, F_j , of a BG can be linearly-coupled to the next segment and can be represented in a matrix form as

$$\begin{bmatrix} R_M(\lambda) \\ S_M(\lambda) \end{bmatrix} = F(\lambda) \begin{bmatrix} R(L) \\ S(L) \end{bmatrix}, \quad F(\lambda) = F_M(\lambda) \cdot F_{M-1}(\lambda) \cdot \dots \cdot F_j(\lambda) \cdot \dots \cdot F_1(\lambda). \quad (2.61)$$

Each of the divided segments, $F_j(\lambda)$, with a grating length of Δz , must satisfy the coupled-mode theory, which results in the following mathematical description [36].

$$F_j(\lambda) = \begin{bmatrix} \cosh[\psi_j(\lambda)\Delta z] - i \frac{\hat{\sigma}_j(\lambda)}{\psi_j(\lambda)} \sinh[\psi_j(\lambda)\Delta z] & -i \frac{\kappa(\lambda)}{\psi_j(\lambda)} \sinh[\psi_j(\lambda)\Delta z] \\ i \frac{\kappa(\lambda)}{\psi_j(\lambda)} \sinh[\psi_j(\lambda)\Delta z] & \cosh[\psi_j(\lambda)\Delta z] + i \frac{\hat{\sigma}_j(\lambda)}{\psi_j(\lambda)} \sinh[\psi_j(\lambda)\Delta z] \end{bmatrix}, \quad (2.62)$$

where the previously defined coupling coefficient, κ , is equal to $\kappa(\lambda) = (\pi/\lambda)\delta n_{eff}$ [Equation (2.8)].

A typical index modulation for a BG, δn_{eff} , is approximately 0.01% of the refractive index of the fiber core [6]. In addition, in a bulk index grating, the materials of the alternating layers differ by little else than the small difference in index, and the thermo-optic coefficients, dn/dT , of the two layers can be expected to be nearly identical. Hence, it is reasonable to assume that the index modulation is invariant with temperature and that any possible change in the modulation is negligible compared to the thermally-driven change of the fiber core index material.

Considering the thermally-driven index shift, the “new” index of refraction for each segment of the grating, $n_{eff2,j}$ can be expressed as

$$n_{eff2,j} = n_{eff1} + \frac{dn}{dT} \Delta T_j. \quad (2.63)$$

Similarly, the “new” period of the grating element caused by thermal expansion is

$$\Lambda_{2,j} = \Lambda_1(1 + \alpha \Delta T_j). \quad (2.64)$$

Using Equations (2.63) and (2.64), the “dc” coupling coefficient for a specified element, $\hat{\sigma}_j$, can be written as

$$\hat{\sigma}_j(\lambda) = \frac{2\pi n_{effj}}{\lambda} - \frac{\pi}{\Lambda_j} + i \frac{\hat{a}}{2} = \frac{2\pi}{\lambda} \left(n_{eff1} + \frac{dn}{dT} \Delta T_j \right) - \frac{\pi}{\Lambda_1(1 + \alpha \Delta T_j)} + i \frac{\hat{a}}{2}, \quad (2.65)$$

and the parameter, ψ_j , can be expressed as

$$\begin{aligned} \psi_j(\lambda) &= \sqrt{\kappa^2(\lambda) - \hat{\sigma}_j^2(\lambda)} \\ &= \sqrt{\left(\frac{\pi}{\lambda} \delta n_{eff} \right)^2 - \left[\frac{2\pi}{\lambda} \left(n_{eff1} + \frac{dn}{dT} \Delta T_j \right) - \frac{\pi}{\Lambda_1(1 + \alpha \Delta T_j)} + i \frac{\hat{a}}{2} \right]^2}. \end{aligned} \quad (2.66)$$

Substituting $\hat{\sigma}_j$ and ψ_j into Equation (2.62), defines all the terms of the matrix, F_j .

Using the boundary conditions ($R(0) = 1$ and $S(L) = 0$) [36], the amplitude of the forward moving wave, $R_M(\lambda)$, and backward moving wave, $S_M(\lambda)$, at the inlet of the PFBG can be obtained. The reflectivity spectrum can then be found as

$$\rho(\lambda) = \frac{|S_M(\lambda)|^2}{|R_M(\lambda)|^2}. \quad (2.67)$$

With the reflectivity determined, it is possible to obtain the reflected power spectrum, $P_{ref}(\lambda)$, as the product of the incident optical power and the reflectivity. Mathematically, it can be expressed in a simple form as

$$P_{ref}(\lambda) = P_{inc} \overline{P(\lambda)} \rho(\lambda). \quad (2.68)$$

2.4. THERMO-OPTICAL BEHAVIOR OF PMMA-BASED PFBG

To illustrate and concretize the thermo-optic behavior analyzed and described in Section 2.3, the present section will focus on the specific characteristics of a PFBG fabricated in polymethylmethacrylate (PMMA), and illuminated by a broad-band LED and a narrow-band SM LD, respectively. Subsection 2.4.1 describes the properties of the selected PMMA-based PFBG and the light sources. Subsection 2.4.2 presents the axial optical power variation, determined by the modified coupled-mode equations, through the PMMA PFBG. Subsections 2.4.3 and 2.4.4 apply the previously derived thermo-optic relations to the determination of the thermally-driven optical characteristics of the PMMA PFBG with LED and SM LD illumination. The subsequent subsection discusses the thermo-optical performance of the PFBG illuminated with other light sources.

TABLE 2.1.
Properties and geometry of PMMA-based polymer fiber Bragg grating.

Parameter	Symbol	Value
Radius of core	r_{co}	3.5 μm
Length	L	1 cm
Grating period	Λ	530.7 nm
Thermal conductivity	k	0.2 $\text{W m}^{-1} \text{K}$
Coefficient of thermal expansion	α	$73 \times 10^{-6} \text{K}^{-1}$
Absorption coefficient	\hat{a}	11.513 m^{-1}
Thermo-optical coefficient	dn/dT	$-1.1 \times 10^{-4} \text{K}^{-1}$
Refractive index of core	n_{co}	1.49
Refractive index of cladding	n_{cl}	1.48
Index modulation	δn_{eff}	7.244×10^{-5}
Effective refractive index	n_{eff}	1.4853
Bragg wavelength	λ_B	1576.5 nm
Coupling coefficient at Bragg wavelength	κ_B	144.36 m^{-1}
Maximum reflectivity	ρ_{max}	0.8
Generalized frequency	V	2.404
Generalized guide index	b	0.5307
Power confinement factor	Γ	0.8265
Beam radius	w	3.7402 μm

2.4.1. Description of a PMMA-Based PFBG and Light Sources

In order to characterize the thermo-optical behavior of a PFBG, a PMMA PFBG, described in the literatures [6,39,40] was chosen. The selected PFBG was fabricated by the phase-mask technique. The detailed fabrication procedure can be found in [6,39,40]. The Bragg wavelength (λ_B), the grating period (Λ), the effective index (n_{eff}), and the maximum reflectivity (ρ_{max}) are 1576.5 nm, 530.7 nm, 1.4853, and 0.8, respectively. Table 2.1 shows all the inherent and derived parameters of the chosen PFBG, including the material properties and the structural, as well as optical parameters.

Typical power spectra for LED and SM LD light sources were depicted in Figure 2.14, which shows the specific power spectra of the LED and SM LD chosen for this analysis. The FWHMs for the LED and the SM LD are 50 nm and 0.026 nm, respectively, and total power is 5 mW for each of the light sources. Consequently, the peak spectral

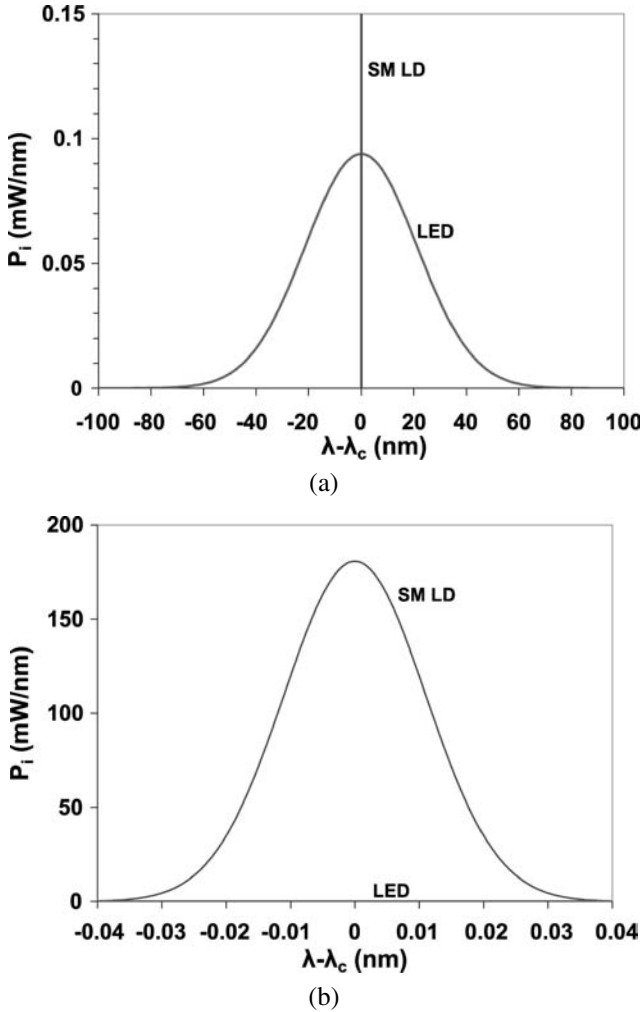


FIGURE 2.14. Power spectra of Light Emitting Diode and Single Mode Laser Diode—5 mW illumination (a) full scale (b) expanded scale.

power density for the SM LD, approximately 180 mW/nm, is nearly 2000 times greater than the 0.1 mW/nm peak spectral power density of the LED.

2.4.2. Power Variation Along the PFBG

Equations (2.32), (2.33), (2.36), (2.37), (2.39) and (2.40) were utilized to calculate the optical power distribution within the PFBG for various detuning values. The PMMA optical parameters, appearing in Table 2.1 and including an absorption coefficient of 11.513 m^{-1} , were used for the calculation. The resulting non-dimensional power variations along the axis of the BG are plotted in Figure 2.15. At the Bragg condition, for which detuning is zero, a significant power gradient exists in both forward and backward moving waves due to the tight energy coupling between the two waves. It is to be noted that, due to the intrinsic absorption of light energy in this non-ideal fiber grating, the reflectivity, ρ (at $z = 0$), at the Bragg condition is about 7% less than the designed reflectivity of 0.8. As attention is shifted away from the Bragg wavelength, detuning increases, resulting in reduced coupling and a progressive approach to simple light wave propagation along the optical fiber. Thus, for large detuning values the incident light experiences no significant reflection and stronger propagation, controlled only by the inherent light absorption in the polymeric medium.

The limiting detuning value, or grating bandwidth (zones I and II in Figure 2.9), beyond which the BG produces no significant reflection, was numerically determined by comparing the optical powers of the forward moving waves at the outlet of the grating obtained by the modified coupled-mode solution [Equations (2.36)] with those evaluated by the simple Beer's law [Equation (2.39)]. Setting the difference in power at the outlet of the grating obtained with these two light propagation models at less than or equal to 1%, yields an absolute value of detuning, $|\delta|$, equal to or greater than $2.25 \times 10^{-6} \text{ nm}^{-1}$. This results in an effective grating bandwidth of $\pm 0.6 \text{ nm}$, i.e., wavelengths beyond this bandwidth propagate freely through the grating.

In this detuned region, only the forward moving wave propagates through the PFBG and any decrease in the power is due exclusively to the intrinsic absorption of light. Con-

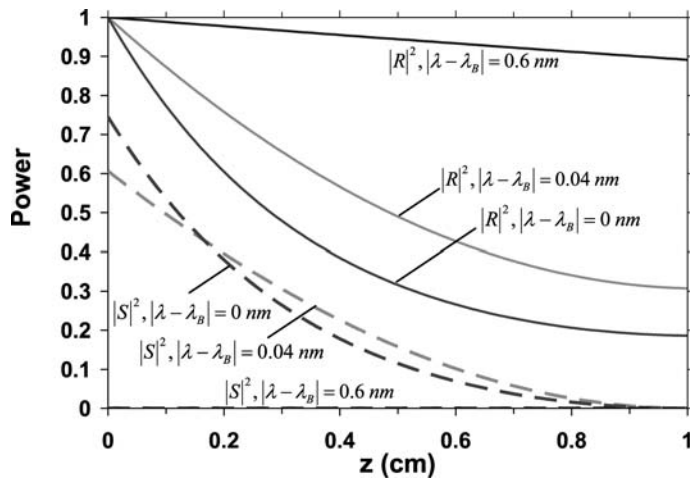


FIGURE 2.15. Incident and reflected power along PMMA fiber Bragg grating.

sequently, for wavelengths that exceed the Bragg wavelengths by $|\lambda - \lambda_B| \geq 0.6 \text{ nm}$, the power variation can be found by Equation (2.39).

2.4.3. Thermo-Optical Behavior of the PFBG–LED Illumination

2.4.3.1. Thermal Analysis The spectral heat generation density, associated with the illumination of the PFBG by an LED, is shown in Figure 2.16, displaying the assumed symmetric Gaussian distribution with respect to the central wavelength and an FWHM of 50 nm. For incident optical powers of 0.5 to 5 mW, maximum spectral heat generation densities attain values of 0.7 to 7 $\text{W cm}^{-3} \text{ nm}^{-1}$. Due to the broad-band illumination provided by the LED, extending substantially beyond the bandwidth of the PFBG, heat generation in the fiber is essentially independent of the reflected wave and can be determined almost exclusively from the inherent absorption of the propagating beam, using Equation (2.44). The resulting exponentially decaying axial profile of heat generation along the PFBG is shown in Figure 2.17 for four different incident optical powers of 0.5, 1, 3, and 5 mW. A more precise calculation of the internal heat generation, using Equation (2.43), revealed that including the reflected, backward moving light wave in the narrow spectral window of the grating bandwidth, $|\lambda - \lambda_B| \leq 0.6 \text{ nm}$ produced a negligible amount of additional heat in the fiber (about 0.01%).

The temperature distribution in a passively-cooled PFBG, resulting from LED illumination, was analytically determined using Equations (2.49) and (2.50) and verified by comparison to results generated by the axisymmetric FEA simulation. The effective heat transfer coefficient, h , on the external surface of the volume representing the fiber was obtained by converting the combined convection and radiation heat transfer coefficient (approximately $10 \text{ W m}^{-2} \text{ K}^{-1}$) on the surface of the fiber, through radial conduction in the cladding and core [41]. The calculated effective heat transfer coefficient, h , for the condition described was $71 \text{ W m}^{-2} \text{ K}^{-1}$, or 335 W/m K when applied to the length of the fiber in the axi-symmetric FEA model.

Figure 2.18 shows the PFBG axial profiles of the excess temperature (determined relative to a 25°C ambient) for the four incident optical powers. The fiber excess tempera-

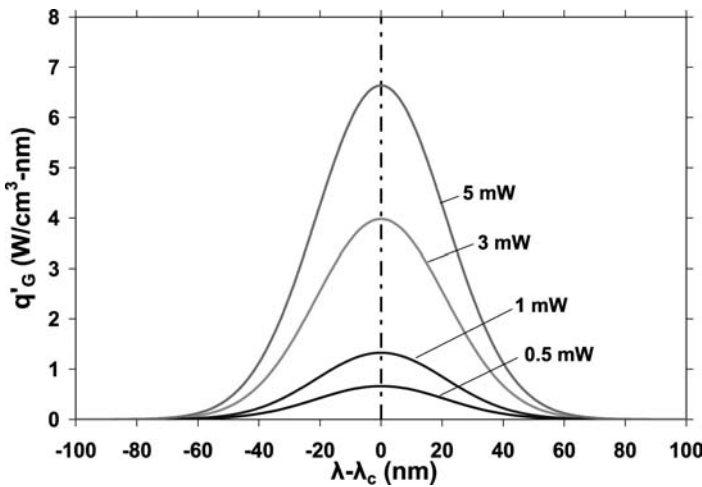


FIGURE 2.16. Spectral heat generation density in PMMA fiber Bragg grating illuminated by Light Emitting Diode.

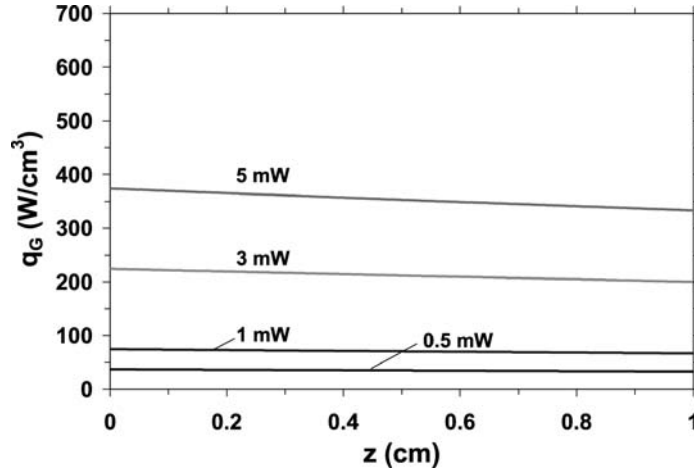


FIGURE 2.17. Heat generation density along PMMA fiber Bragg grating illuminated by Light Emitting Diode.

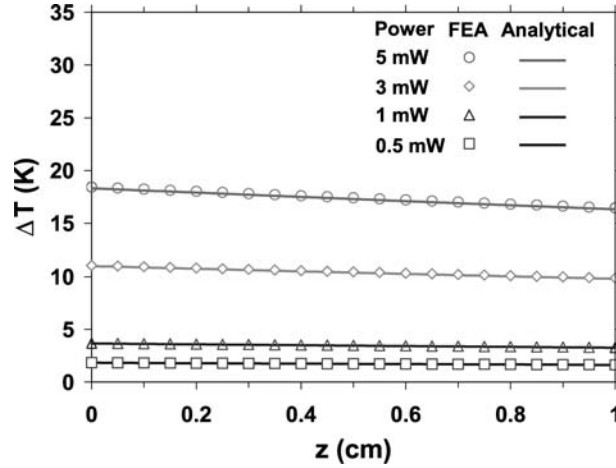


FIGURE 2.18. Analytical and numerical excess temperatures along PMMA fiber Bragg grating illuminated by Light Emitting Diode.

tures vary from 18 K at the inlet of the fiber illuminated with the highest incident power of 5 mW to just 2 K for the 0.5 mW. The analytical and FEA results display the anticipated, though barely discernable, exponential decay and appear to match each other extremely well, typically within 0.7%.

The finite-element model was further utilized to calculate the radial temperature variations in the PFBG. The results are shown in Figure 2.19, where the axial variation of the temperature difference ($T_c - T_{co}$) between the center of the PFBG core (T_c) and the core surface (T_{co}) is plotted. The peak radial temperature differences are seen to range from 0.06 K at 5 mW to 0.01 K at 0.5 mW of incident LED power and thus justify the radially-uniform temperature assumption used in the analytical temperature relations. Figure 2.19 also reveals a slight decrease in the radial temperature difference as the PFBG is traversed from the inlet to the outlet end. It should, nevertheless, be noted that, due to the 7 micron

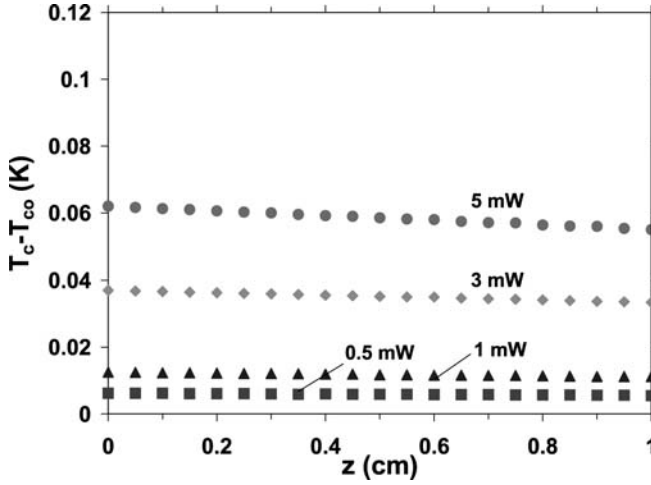


FIGURE 2.19. Radial temperature differences along PMMA fiber Bragg grating illuminated by Light Emitting Diode.

diameter of the PFBG, these radial temperature variations do yield significant temperature gradients.

2.4.3.2. Thermo-Optical Analysis

2.4.3.2.1. Reflectivity Spectrum. In order to obtain the reflectivity spectrum of the specified PFBG associated with the LED, the temperature distribution obtained from Equations (2.49) and (2.50) was integrated with the modified TMM relations [Equations (2.61) and (2.62)]. In the TMM implementation, a total of 200 segments ($\Delta z = 50 \mu\text{m}$) was used with wavelength bands of 0.5 pm.

Figure 2.20 displays the thermally-induced shift in the spectral reflectivity of the specified PFBG illuminated with 5 mW of LED power and operating in an ambient temperature of 25°C. The individual effects of the index change with temperature, (dn/dT) , and the grating period change with temperature, $(d\Lambda/dT)$, were determined.

The results clearly indicate that the thermally-driven index change (thermo-optic) produces a negative shift in the reflectivity spectrum, relative to the incident 1576.5 nm-centered LED light, with the dominant “Bragg” wavelength moving lower by -2.03 nm . The change of the grating period due to thermal expansion results in a positive shift in the reflectivity spectrum, driving the dominant wavelength to higher values by 2.0 nm . The jagged character of the reflectivity spectrum is associated with the spectral dispersion induced by the axially non-uniform PFBG temperature and will be explored in a later section. The combined reflectivity spectrum for the 5 mW illuminated fiber shows a very small total shift in Bragg wavelength (-0.03 nm), with modest spectral dispersion. The previously noted, spectral compensation, which results from the comparable magnitude, though opposite sign of the two individual effects, is in clear evidence in this reflectivity spectrum.

The total reflectivity spectra, including both the thermal expansion and thermo-optic change with temperature, are displayed with an expanded wavelength scale in Figure 2.21, for 0.5 and 5 mW of LED illumination. The total reflectivity spectra show a consistent reflectivity shape with the constant FWHM of 0.12 nm, a maximum reflectivity of 0.74, and a small Bragg wavelength shift in the negative direction for each incident optical power.

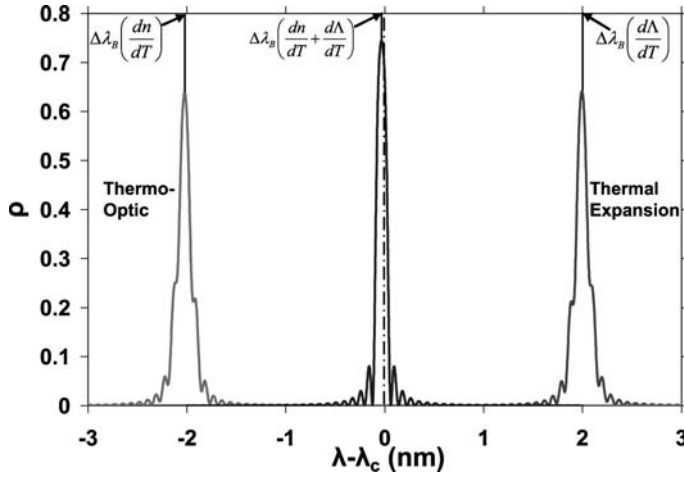


FIGURE 2.20. Thermally-induced Bragg wavelength shifts in PMMA fiber Bragg grating illuminated with a 5 mW Light Emitting Diode—thermo-optic (dn/dT), thermal expansion ($d\Lambda/dT$), and combined effects ($dn/dT + d\Lambda/dT$).

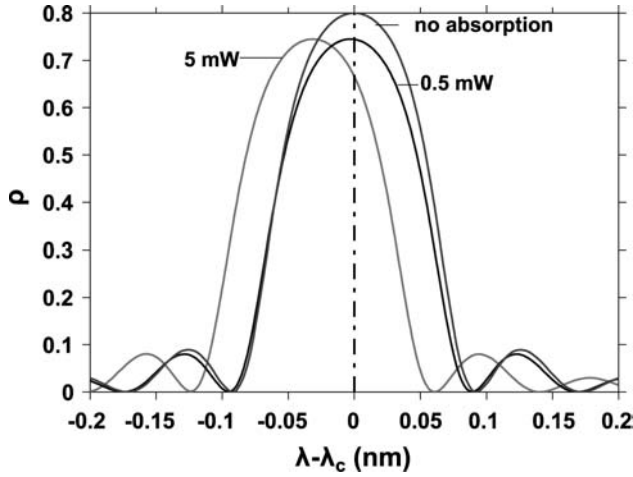


FIGURE 2.21. Reflectivity spectra for Light Emitting Diode illumination of PMMA fiber Bragg grating.

2.4.3.2.2. Reflected Power Spectrum. Although the rigorously evaluated reflectivity spectra provide useful information on the spectral dependence of the reflectivity and the Bragg wavelength shifts, due to the Gaussian spectral distribution of the incident LED illumination, they may not represent the character of the reflected power. To obtain reflected power spectra and the power-based Bragg wavelength shift, it is, thus, necessary to perform a convolution of these two distributions (i.e., Gaussian illumination and coupled-mode reflectivity).

Figure 2.22 shows the reflected power spectra for the four incident optical powers, obtained via a convolution of Equations (2.67) and (2.68), when the ambient is 25°C. Due to the wide-band LED source, the reflected power spectra present similar profiles to those of the reflectivities alone, with nearly identical negative shift in the dominant wavelength.

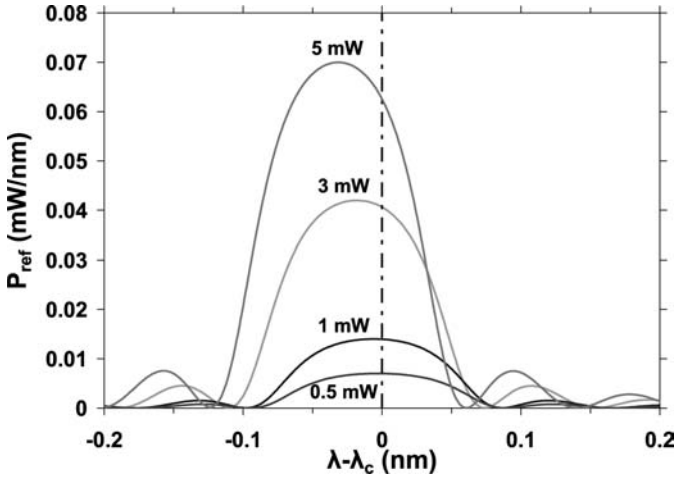


FIGURE 2.22. Reflected power spectra for Light Emitting Diode illumination of PMMA fiber Bragg grating.

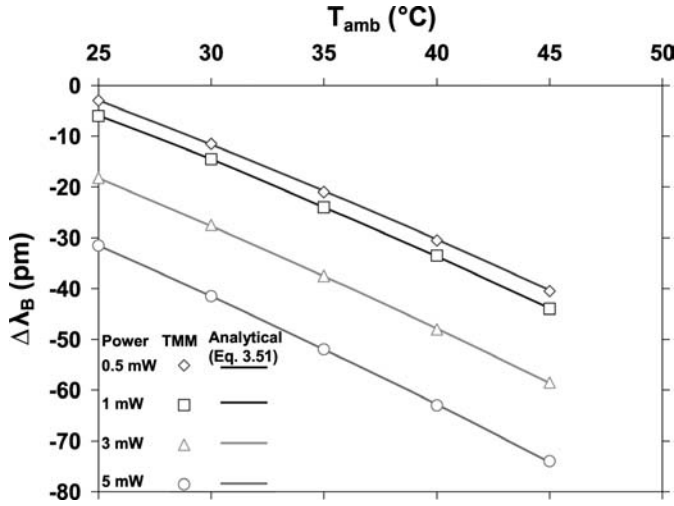


FIGURE 2.23. Bragg wavelength shifts in PMMA fiber Bragg grating illuminated with Light Emitting Diode.

2.4.3.2.3. Parametric Effects on Bragg Wavelength Shifts. The Bragg wavelength shift is, perhaps, the single most important parameter used to characterize the thermo-optical behavior of a PFBG. This Bragg wavelength shift is driven by the temperature change in the PFBG induced by both absorption and the ambient temperature change. Figure 2.23 shows the shifted Bragg wavelengths in an ambient varying from 25°C to 45°C and for four incident optical powers. The results were obtained using both the modified-TMM (the methodology used to produce the spectral reflectivity variations displayed in Figure 2.21) and Equation (2.60), with an axially-averaged PFBG temperature. The analytically determined Bragg wavelength shifts, including the quadratic term in Equation (2.60) and based on the axially-averaged temperatures, are seen to agree very well (typically to within better than 1%), with the values extracted from the more detailed modified TMM methodology.

TABLE 2.2.
Bragg wavelength shifts in PMMA-based polymer fiber Bragg grating with Light Emitting Diode illumination.

Ambient temperature, T_{amb}	Incident optical power, P_{inc} (mW)	Average excess temperature, $\overline{\Delta T}$ (K)	Transfer Matrix Method (pm)	Quadratic Eq. (2.60) (pm)	Linear Eq. (2.55) (pm)
25	0.5	1.73	-3	-2.9	-2.9
25	1	3.46	-6	-5.9	-5.8
25	3	10.38	-18.2	-18.3	-17.3
25	5	17.31	-31.5	-31.5	-28.9
30	0.5	6.73	-11.5	-11.6	-11.2
30	1	8.46	-14.5	-14.5	-14.1
30	3	15.38	-27.5	-27.7	-25.7
30	5	22.31	-41.5	-41.5	-37.3
35	0.5	11.73	-21	-20.8	-19.6
35	1	13.46	-24	-24	-22.5
35	3	20.38	-37.5	-37.6	-34.0
35	5	27.31	-52	-52	-45.6
40	0.5	16.73	-30.5	-30.3	-27.9
40	1	18.46	-33.5	-33.7	-30.8
40	3	25.38	-48	-47.9	-42.4
40	5	32.31	-63	-62.8	-53.9
45	0.5	21.73	-40.5	-40.3	-36.3
45	1	23.46	-44	-43.9	-39.2
45	3	30.38	-58.5	-58.6	-50.7
45	5	37.31	-74	-74.2	-62.3

The less accurate linear superposition formulation, given by Equation (2.55), yields a 2% to 18% discrepancy with those determined by the TMM.

The Bragg wavelength shifts calculated by all 3 methods are presented in Table 2.2. The significant effect of ambient temperatures on the shifts in Bragg wavelength is evident. For example, the effect of 15 K of ambient temperature rise is almost equivalent to that of 10 fold power increase from 0.5 mW to 5 mW.

Figure 2.24 presents the estimated shifts of Bragg wavelengths by TMM with non-uniform temperature, TMM with uniform temperature, quadratic analytical method, and linear analytical method. For these condition, the Bragg wavelength shifts are seem to be governed mainly by the average temperatures and the temperature gradients have a negligible effect.

2.4.4. Thermo-Optical Behavior of the PFBG–SM LD Illumination

2.4.4.1. Thermal Analysis Unlike the modeling approach used with the broad-band LED light source, heat generation associated with narrow-band SM LD illumination (FWHM of just 0.026 nm) strongly depends on the coupling between the forward and backward moving waves within the bandwidth of the PFBG, previously shown to extend well beyond the spectral bandwidth of the incident SM LD light. Since the Bragg wavelength shift can be expected to be of the same magnitude as the FWHM, the thermal and thermo-optical model (the modified TMM) associated with the illumination of the SM LD must be solved in a coupled way.

The spectral bandwidth of the chosen SM LD light source is 0.026 nm, which is expected to be smaller than the boundary of zone I. Consequently, the closed-form solution

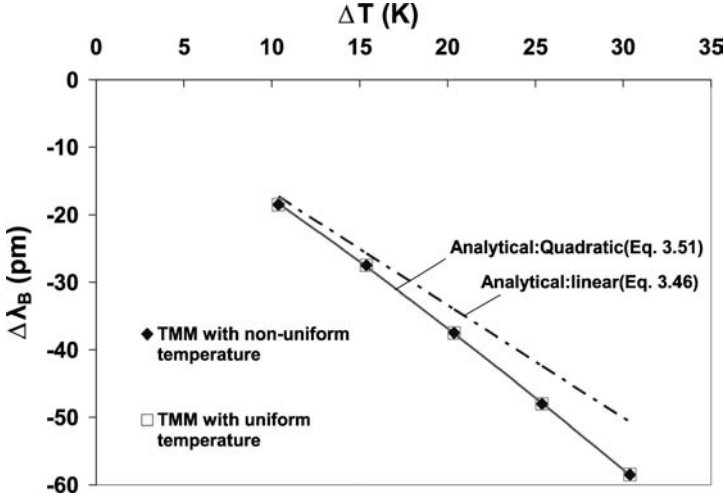


FIGURE 2.24. Transfer matrix method Bragg wavelength shifts—axially uniform and non-uniform temperature.

of the coupled-mode equation [Equations (2.32) and (2.33)] was used to obtain analytically the power variation in the grating. As in the LED analysis, a total of 200 segments ($\Delta z = 50 \mu\text{m}$) was used with a wavelength band of $0.5 \mu\text{m}$ for the discretization required to apply the TMM methodology.

In order to consider the simultaneous variance of the Bragg wavelength and heat generation, the fully coupled model must satisfy an energy balance $P_{inc} - P_{out} = q_G$, where P_{inc} , P_{out} , and q_G are the incident total optical power, the total optical power at the outlet, and the generated total heat, respectively. However, the optical power and the heat generation depend on the Bragg wavelength, which in turn, depends on the temperature. To deal with this additional interdependence, an iterative procedure, outlined in Figure 2.25, was established to determine the Bragg wavelength at which this energy balance could be attained.

Figure 2.26 shows the spectral heat generation density, associated with the SM LD illumination of the PFBG, for the four optical powers. Due to the narrow-band SM LD source, a much larger spectral heat generation density, than obtained with the LED, is evident at the same total illumination rates. It may also be noticed that the spectral distribution of the heat generation is slightly asymmetric about the central wavelength of the incident light, thus, differing from the perfectly symmetric distribution with the LED light source. This small, though observable shift in the spectral distribution of generated heat, can be related to the combination of the reduced coupling between the incident and reflected wave as well as the strong spectral variation of the incident light.

Figure 2.27 presents the variation in heat generation, obtained from the solution of Equation (2.45) along the axis of the PFBG, associated with the illumination of the narrow-band SM LD, for the four optical powers. It should be noted that the heat generation density of the SM LD at the inlet, peaking at 640 W/cm^3 for 5 mW , is approximately 70% greater than that of the LED. As a result, the axial heat generation gradient of the SM LD becomes much larger.

Since all of the SM LD power, with a FWHM of 0.026 nm , is contained well within the bandwidth of the PFBG, nearly the entire spectrum of the incident wave experiences Bragg reflections from the grating, drastically reducing the amount of light propagating to

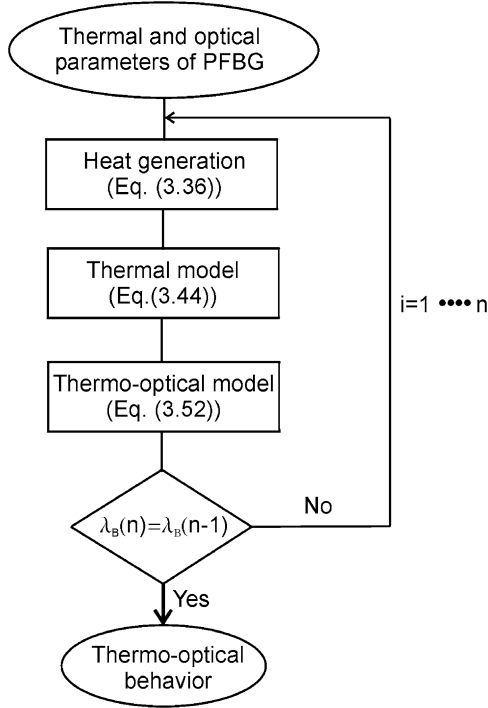


FIGURE 2.25. Iterative solution procedure—fully coupled thermo-optical analysis.

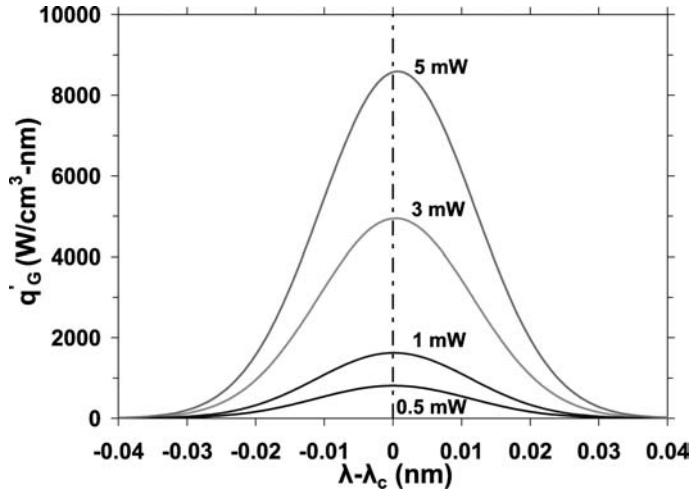


FIGURE 2.26. Spectral heat generation density in PMMA fiber Bragg grating illuminated by Single Mode Laser Diodes.

the outlet end of the grating. Using these internal heat generation profiles, it is now possible to determine the temperature variations within the PMMA FBG using Equations (2.53) and (2.54) as well as the previously described finite-element model. As mentioned earlier, the closed-form solution of the coupled-mode equation is valid in the entire spectral window

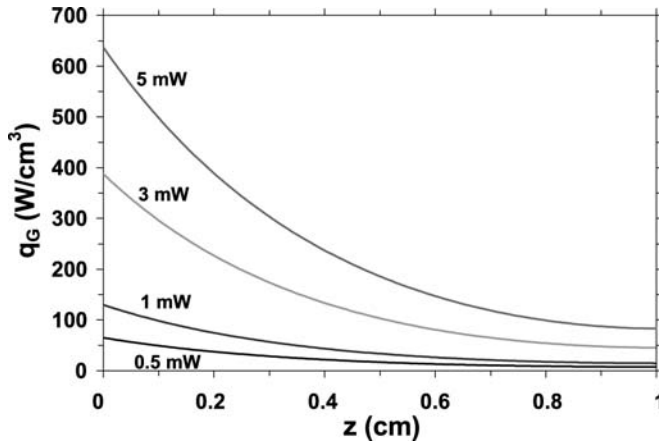


FIGURE 2.27. Heat generation density along PMMA fiber Bragg grating illuminated by Single Mode Laser Diode.

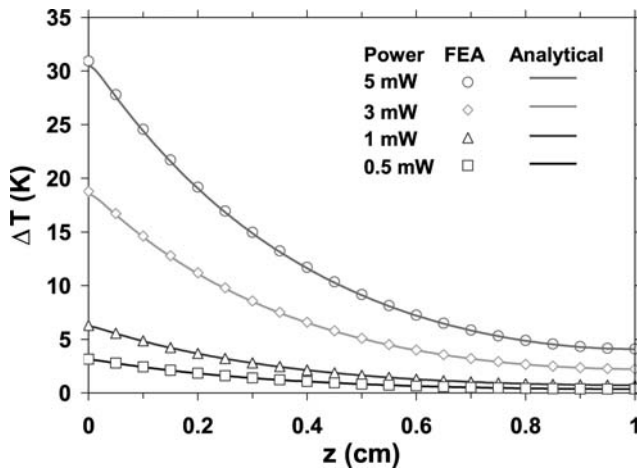


FIGURE 2.28. Analytical and numerical excess temperatures along PMMA fiber Bragg grating illuminated by Single Mode Laser Diode.

for the chosen SM LD. Hence, the integral term associated only with $\lambda_2 \leq \lambda \leq \lambda_3$ (zone I) was evaluated in the temperature solutions of Equations (2.53) and (2.54).

Figure 2.28 shows the PFBG axial profiles of the excess temperature (determined relative to a 25°C ambient) for the four incident optical powers. The results reveal that the inlet of the SM LD illuminated PFBG experiences significant heating, reaching an excess temperature of 31 K at 5 mW and 3 K even at just 0.5 mW of incident power, significantly higher than the peak temperatures induced by the previously described LED illumination. As expected from the highly non-uniform heat generation rate for the SM LD, displayed in Figure 2.27, a large axial temperature gradient, varying from nearly 27 K/cm at 5 mW to just 3 K/cm at 0.5 mW of incident power, is generated in the grating.

The results obtained with the finite-element simulation of the SM LD illuminated PFBG are also shown in Figure 2.28. They agree very well with the analytical results,

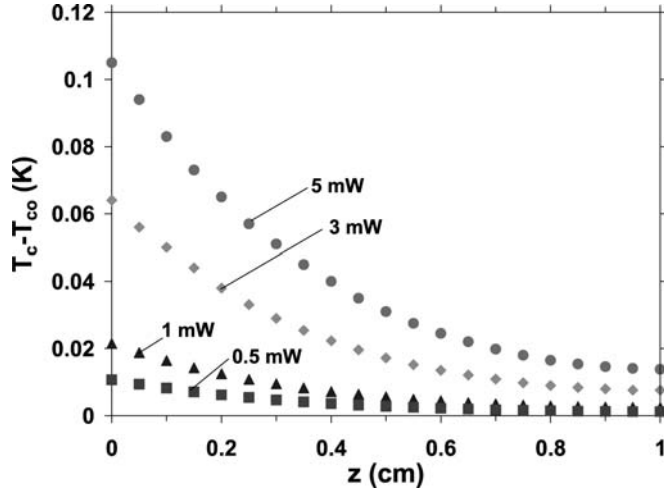


FIGURE 2.29. Radial temperature differences along PMMA fiber Bragg grating illuminated by Single Mode Laser Diode.

typically to within 1%. Further reinforcing the importance of the strong optical coupling between the incident and reflected waves, which occurs with the narrow-band light source, the average temperature rise of the specified PMMA PFBG induced by SM LD illumination at 5 mW and 0.5 mW is approximately 30% lower than the comparable values for the LED illumination.

Figure 2.29 shows the radial temperature difference between the center of the PFBG core (T_c) and the core surface temperature (T_{co}) along the PFBG. The maximum radial temperature difference lies below 0.11 K at the inlet of the grating and decreases axially to below 0.02 K for the highest light intensity of 5 mW, with similar profiles and even lower radial temperature differences for the lower illumination powers. Thus, the FEA results validate the one-dimensional heat conduction assumption used in the analytical thermal model for the narrow-band light source.

2.4.4.2. Thermo-Optical Analysis

2.4.4.2.1. Reflectivity Spectrum. Figure 2.30(a) shows the total reflectivity spectra for the maximum and minimum incident SM LD powers considered, as well as the no absorption case, all calculated with Equation (2.61), which include both the effects of the thermally-driven index shift and the grating period change due to thermal expansion. It is worth noting that the reflectivity spectrum for the SM LD does not display the multiple side lobes, which were present in the reflectivity spectrum of the LED. However, when compared to the “central” region around the Bragg wavelength for both the LED and SM LD illumination, shown in a magnified view in Figure 2.30(b), it becomes apparent that this difference can be related directly to the narrow-band of the SMLD light source, which contains all the incident light well within the grating bandwidth of the PMMA based PFBG. From an examination of Figure 2.30 it is also possible to deduce the Bragg wavelength shift based on the wavelength of the peak reflectivity of the incident light for the two limiting SM LD illuminations.

Table 2.3 provides additional Bragg wavelength shift values, extracted from reflectivity spectra (TMM), and compares these to the values predicted from Equations (2.60) and (2.55). The Bragg wavelength shifts estimated by Equation (2.60), using the quadratic

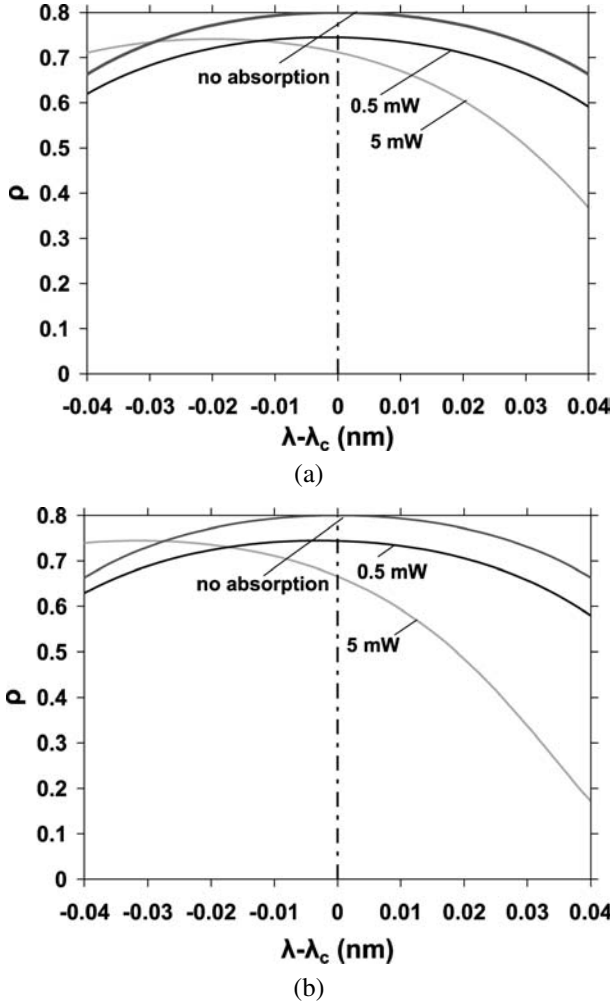


FIGURE 2.30. Narrow-band reflectivity spectra for PMMA fiber Bragg grating—(a) Single Mode Laser Diode illumination, (b) Light Emitting Diode illumination.

relation, shows generally good agreement with those evaluated by the TMM method, falling typically within 3% of the TMM values. On the contrary, estimates using Equation (2.55), based on a simple linear superposition of the thermo-optic and strain terms, generally show a 3 to 10% discrepancy with the TMM results.

It is to be noted that at the same incident power levels, the SM LD results in nearly 30% smaller Bragg wavelength shifts compared to those produced by the LED light source. This reduction in $\Delta\lambda_B$ can be explained by the approximately 30% lower average temperature rise for the PMMA grating illuminated by the SM LD.

2.4.4.2.2. Reflected Power Spectrum. The reflectivity of a BG is defined as the ratio of the reflected optical power to the incident optical power at the inlet of the PFBG (at $z = 0$). To obtain this reflectivity, it is again necessary to perform a convolution of the incident spectrum with the calculated spectral reflectivity, which yields the reflected power spectra

TABLE 2.3.
Bragg wavelength shifts in PMMA-based polymer fiber Bragg grating with Single Mode Laser Diode illumination.

Ambient temperature, T_{amb}	Incident optical power, P_{inc} (mW)	Average excess temperature, $\overline{\Delta T}$ (K)	Transfer Matrix Method (pm)	Quadratic Eq. (2.60) (pm)	Linear Eq. (2.55) (pm)
25	0.5	1.12	-1.5	-1.9	-1.9
25	1	2.24	-3.5	-3.8	-3.7
25	3	6.83	-11	-11.8	-11.4
25	5	11.85	-20	-21	-19.8
30	0.5	6.14	-10.5	-10.6	-10.3
30	1	7.29	-12.5	-12.6	-12.2
30	3	12.15	-21	-21.6	-20.3
30	5	17.98	-32	-32.8	-30.0
35	0.5	11.18	-19.5	-19.7	-18.7
35	1	12.39	-21.5	-22	-20.7
35	3	17.79	-32	-32.4	-29.7
40	0.5	16.27	-29.5	-29.4	-27.2
40	1	17.6	-32	-32	-29.4
45	0.5	21.4	-39.5	-39.6	-35.7

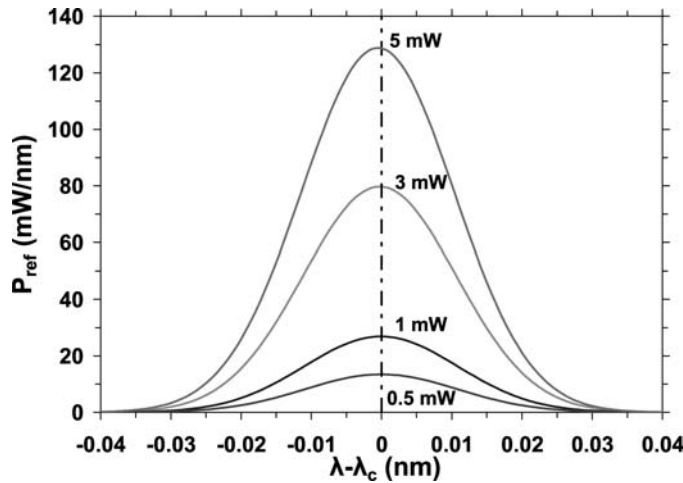


FIGURE 2.31. Reflected power spectra for Single Mode Laser Diode illumination of PMMA fiber Bragg grating.

and then integrate this over the bandwidth of the light source to obtain the total reflected power and grating reflectivity.

This procedure was followed using Equations (2.67) and (2.68). The results are displayed in Figure 2.31, showing the reflected power spectra associated with the four optical powers. The shifts of wavelengths at maximum reflected powers (*apparent Bragg wavelength shift*) with the SM LD are much smaller than those based on the peak reflectivity values (*true Bragg wavelength shift*) and summarized in Table 2.4. Furthermore, comparison of the “power” $\Delta\lambda_B$ values for the SM LD and the LED, reveals the shifts with the narrow-band light source to be far smaller than with the broad-band LED light source.

TABLE 2.4.
True and apparent Bragg wavelength shifts in PMMA-based polymer fiber Bragg grating
illuminated with Single Mode Laser Diode.

Ambient temperature, T_{amb}	Incident optical power, P_{inc} (mW)	Average excess temperature, ΔT (K)	True Bragg wavelength shift by Transfer Matrix Method (pm)	Apparent Bragg wavelength shift by Transfer Matrix Method (pm)
25	0.5	1.12	-1.5	0
25	1	2.24	-3.5	0
25	3	6.83	-11	-0.5
25	5	11.85	-20	-0.5
30	0.5	6.14	-10.5	0
30	1	7.29	-12.5	-0.5
30	3	12.15	-21	-0.5
30	5	17.98	-32	-0.5
35	0.5	11.18	-19.5	-0.5
35	1	12.39	-21.5	-0.5
35	3	17.79	-32	-1
40	0.5	16.27	-29.5	-1
40	1	17.6	-32	-1
45	0.5	21.4	-39.5	-1.5

For example, the wavelength shifts at the maximum reflected power with 5 mW of LED and SM LD illumination are 31.5 pm and 0.5 pm, respectively. This much reduced Bragg wavelength shift with the SM LD is mainly due to the strong spectral dependence of the incident power. For wavelength shifts outside the FWHM band of the incident light, the incident power sharply decreases so that the maximum reflected power can only occur near the center of the grating bandwidth.

2.4.4.2.3. Parametric Effects on $\Delta\lambda_B$. Figure 2.32 demonstrates the difference between the true Bragg wavelength, λ_B (the wavelength at the maximum reflectivity), and the apparent Bragg wavelength, λ'_B (the wavelength at the maximum reflected power measured by an optical spectrum analyzer), for an incident power of 3 mW and an ambient temperature of 35°C. As shown in Figure 2.32, the maximum reflected power occurs at $\lambda - \lambda_c = -2$ pm while the maximum reflectivity is found at $\lambda - \lambda_c = -33$ pm, resulting in a considerable difference between the true and apparent Bragg wavelength shift for these specific conditions. Table 2.4 provides further support for these conclusions, showing this variance between the apparent and true Bragg wavelength for a variety of SM LD operating conditions.

Figure 2.33 shows the Bragg wavelengths shifts with ambient temperature for the four optical powers, revealing the significant effect of ambient temperature rise on the Bragg wavelength shift. The effect is even more significant than in the case of the LED light source. An ambient temperature rise of approximately 10 K is seen to produce a Bragg wavelength shift almost equivalent to that resulting from a factor of 10 increase in the incident optical power. A 15 K ambient temperature rise would be needed to produce the same effect in a PFBG subjected to LED illumination.

Despite the relative simplicity of the analytical equation, Equation (2.60) predicts the wavelength shift faithfully; the maximum discrepancy with the shift predicted by the modified TMM is less than 1 pm. The variance between the apparent and true Bragg wavelengths induced by a change in ambient temperature is presented in Figure 2.34. It clearly

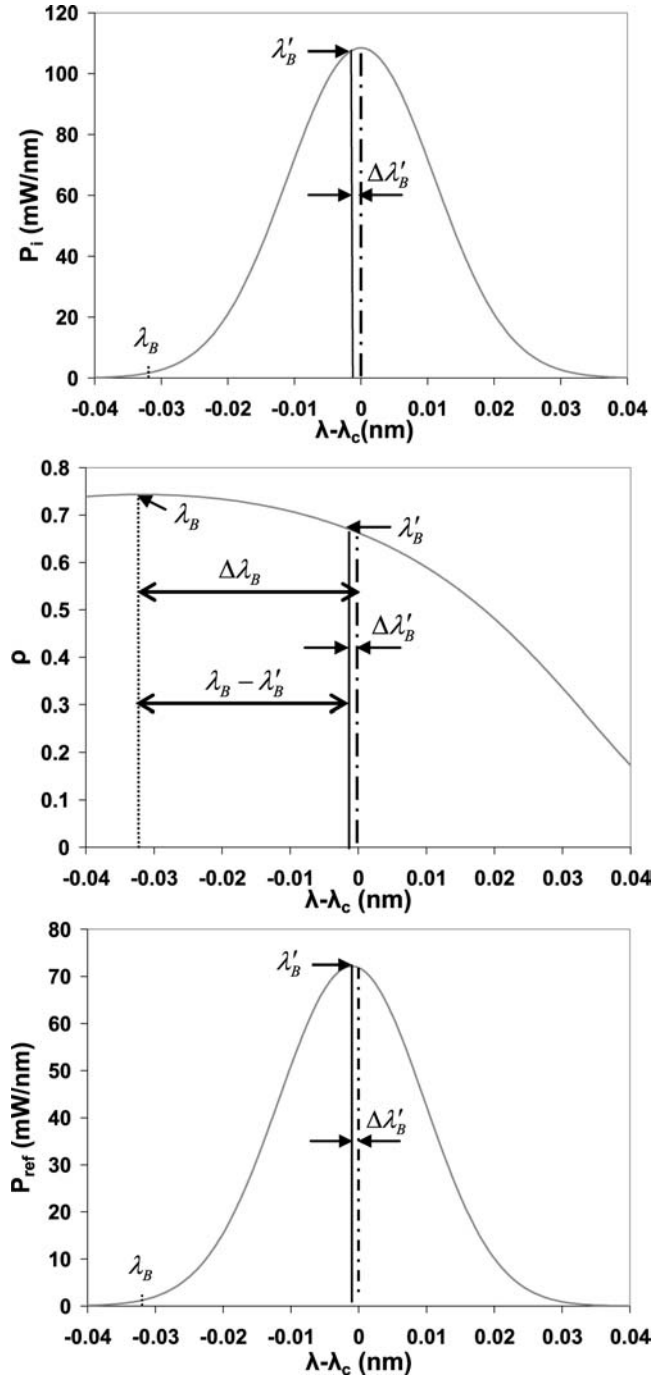


FIGURE 2.32. Apparent and true Bragg wavelength shifts in PMMA fiber Bragg grating illuminated with 3 mW Single Mode Laser Diode.

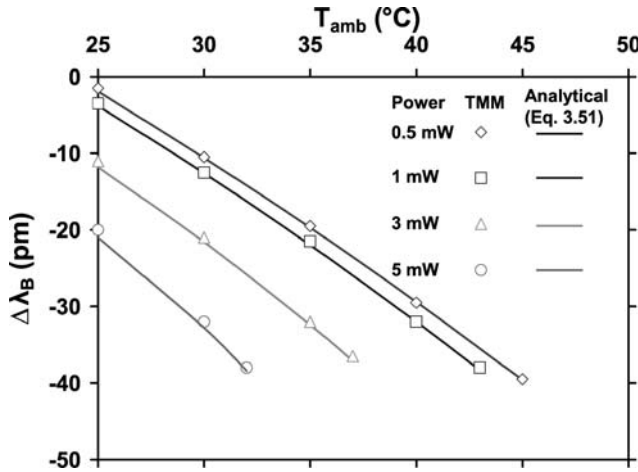


FIGURE 2.33. Bragg wavelength shifts in PMMA fiber Bragg grating illuminated with Single Mode Laser Diode.

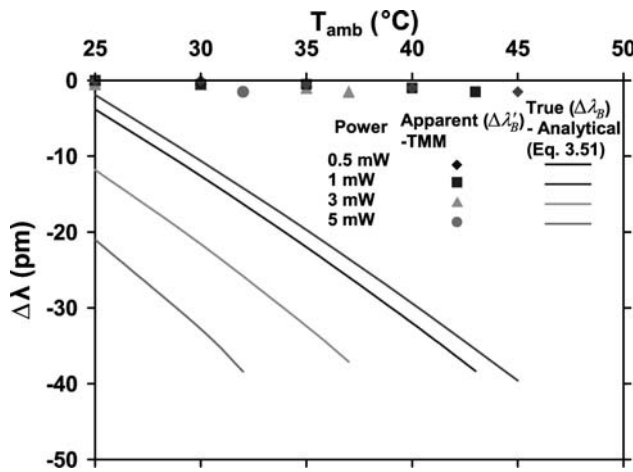


FIGURE 2.34. True and apparent Bragg wavelength shifts induced by ambient temperature and Single Mode Laser Diode illumination.

demonstrates that the considerable discrepancy between the apparent and true Bragg wavelength exists when the SM LD is used. This was caused by the sharp spectral dependence of the power density, as previously discussed.

2.4.5. Thermo-Optical Behavior of the PFBG Associated with Other Light Sources

In the preceding sections, the thermo-optical behavior of the PFBG, induced by illumination from typical SM LD's and LED's, respectively, was characterized. In solving the coupled-mode equations analytically, the entire spectrum of the chosen SM LD was found to lie well within the approximately determined bandwidth of the grating, using a range of engineering criteria for the effective bandwidth of the BG. Alternatively, heating of the PFBG by the broad spectrum of the LED, which considerably exceeded the similarly-

defined grating bandwidth, was found to follow the relatively simple Beer's Law condition. However, it must be recognized that these two illumination sources represent the "narrow-band" and "broad-band" limits, respectively, and that not all light sources result in closed form solutions of the thermo-optic relations.

Furthermore, more severe limitations are imposed by the particular mathematical solution of the simplified first order coupled-differential equations, which assumed a slowly varying amplitude envelope of the incident and reflected waves and the occurrence of energy coupling, between the two counter-propagating waves, in near the Bragg resonance [28]. It is to be noted that relaxation of these assumptions in the coupled-mode theory produces, two-dimensional, second order, coupled-partial differential equations, whose solution would require more advanced numerical methods than used in the foregoing.

2.5. CONCLUDING REMARKS

The foregoing described the development of a thermo-optic modeling methodology for characterizing the behavior of a PFBG, in which intrinsic heating—caused by light absorption in the fiber—is significant. Detailed numerical simulations of both the optical and temperature fields, including the impact of axial temperature gradients, were presented to yield the axial and radial spectral power variation in the forward and backward moving waves, from which the reflectivity and the Bragg wavelength shift can be determined. Analytical approximations of the temperature field and the resulting Bragg wavelength shift, produced by light absorption, as well as ambient temperature variations, were derived and compared to the results of the detailed numerical simulations.

This methodology was applied to a PMMA FBG illuminated alternately with a broad-band Light Emitting Diode (LED) and narrow-band Single Mode Laser Diode (SMLD) light source in the 0.5 mW to 5 mW range. The resulting high volumetric heating rate was seen to produce significant temperature rise and strong temperature gradients, especially with the SM LD illumination, in the grating. The induced temperature field resulted in a increase in the length but to a nearly comparable compensating decrease in the effective index of refraction of the PMMA grating, greatly reducing the Bragg wavelength shift and yielding nearly athermal grating behavior.

Detailed evaluation of the numerical results, obtained with the TMM, revealed that in the PMMA grating, the "chirp," produced by the absorption induced temperature gradients, led to some additional features in the reflectivity spectrum, but did not materially affect the Bragg wavelength shift ($\Delta\lambda_B$) of the PFBG. Consequently, an analytical relation—based on the use of both linear and quadratic excess average temperature terms—was seen to yield $\Delta\lambda_B$ values that are nearly indistinguishable from the more rigorous numerical solution. The TMM simulation has also identified a Bragg shift anomaly for narrow-band illumination, with the reflectivity based shift far larger than power-based shift in the PMMA grating.

REFERENCES

1. L. Eldada and L. Shacklette, Advances in polymer integrated optics, IEEE Journal of Selected Topics in Quantum Electronics, 6, pp. 54–68 (2000).
2. K.O. Hill and G. Meltz, Fiber Bragg grating technology fundamentals and overview, Journal of Lightwave Technology, 15, pp. 1263–1276 (1997).

3. K.O. Hill, B. Malo, et al., Bragg Gratings fabricated in monomode photosensitive optical fiber by UV exposure through a phase mask, *Applied Physics Letters*, 62, pp. 1035–1037 (1993).
4. K.O. Hill, Y. Fujii, D.C. Johnson, and B.S. Kawasaki, Photosensitivity in optical fiber waveguides, *Applied Physics Letters*, 32, pp. 647–649 (1978).
5. A. Othonos, *Fiber Bragg Gratings-fundamentals and Applications in Telecommunications and Sensing*, Artech House, Boston (1999).
6. Z. Xiong, G.D. Peng, B. Wu, and P.L. Chu, Highly tunable Bragg gratings in single-mode polymer optical fibers, *IEEE Photonics Technology Letters*, 11, pp. 352–354 (1999).
7. Y.-J. Rao, D.J. Webb, D.A. Jackson, L. Zhang, and I. Bennion, In-Fiber Bragg-grating temperature sensor system for medical applications, *Journal of Lightwave Technology*, 15, pp. 779–785 (1997).
8. E.D.J. Smith, B.A. Patterson, R.J. Webster, P.A. Krug, S.K. Jones, and D.D. Sampson, Engineering a portable quasi-distributed fibre-Bragg-grating temperature sensing system for clinical hyperthermia, *Optical Fiber Sensors Conference Technical Digest*, 2002, OFS 2002, 15th, 6–10 May 2002, pp. 269–272.
9. B.A. Patterson, D.D. Sampson, et al., In vivo quasi-distributed temperature sensing with fibre Bragg gratings, *Lasers and Electro-Optics*, 2001, CLEO '01, Technical Digest. Summaries of papers presented at the conference on, 6–11 May 2001, pp. 402–403.
10. A.V. Koulaxouzidis, M.J. Holmes, C.V. Roberts, and V.A. Handerek, A shear and vertical stress sensor for physiological measurements using fibre Bragg gratings, *Engineering in Medicine and Biology Society*, 2000, Proceedings of the 22nd Annual International Conference of the IEEE, Volume 1, 23–28 July 2000, pp. 55–58.
11. N.E. Fisher, J. Surowiec, et al., In-fibre Bragg gratings for ultrasonic medical applications, *Measurement Science & Technology*, 8, pp. 1050–1054 (1997).
12. T. Katchalski and E. Teitelbaum, Towards ultra-narrow bandwidth polymer-based resonant grating waveguide structures, *Applied Physics Letters*, 84, pp. 472–474 (2004).
13. W.C. Wang, M. Fisher, et al., Phase-shifted Bragg grating filters in polymer waveguides, *IEEE Photonics Technology Letters*, 15, pp. 548–550 (2003).
14. J.-W. Kang, M.-J. Kim, et al., Polymeric wavelength filters fabricated using holographic surface relief gratings on azobenzene-containing polymer films, *Applied Physics Letters*, 82, pp. 3823–3825 (2003).
15. H. Zou, K.W. Beeson, and L.W. Shacklette, Tunable planar polymer Bragg gratings having exceptionally low polarization sensitivity, *Journal of Lightwave Technology*, 21, pp. 1083–1088 (2003).
16. T. Augustsson, Proposal of a Bragg grating assisted MMIMI-coupler for tunable add-drop multiplexing, *IEEE Photonics Technology Letters*, 13, pp. 1011–1013 (2001).
17. A. Sato, S. Atsushi, et al., Holographic edge-illuminated polymer Bragg gratings for dense wavelength division optical filters at 1550 nm, *Applied Optics*, 42, pp. 778–784 (2003).
18. J.-F. Viens, C. Callender, et al., Compact wide-band polymer wavelength-division multiplexers, *IEEE Photonics Technology Letters*, 12, pp. 1010–1012 (2000).
19. L. Eldada, Y. Shing, et al., Integrated multichannel OADM's using polymer Bragg grating MZI's, *IEEE Photonics Technology Letters*, 10, pp. 1416–1418 (1998).
20. S. Tang, Y. Tang, et al., Fast electrooptic Bragg grating couplers for on-chip reconfigurable optical waveguide interconnects, *IEEE Photonics Technology Letters*, 16, pp. 1385–1387 (2004).
21. T. Erdogan, Fiber grating spectra, *Journal of Lightwave Technology*, 15, pp. 1277–1294 (1997).
22. C.-L. Chen, *Elements of Optoelectronics and Fiber Optics*, Irwin, Chicago, 1996.
23. T. Tamir, *Guided-wave Optoelectronics*, Springer-Verlag, New York, 1990.
24. D. Lee, *Electromagnetic Principles of Integrated Optics*, John Wiley and Sons, New York, 1986.
25. P.K. Cheo, *Fiber Optics and Optoelectronics*, Prentice-Hall, Englewood Cliffs, NJ, 2nd ed., 1990.
26. Product specification sheets of the Mitsubishi DFB laser diodes (ML9XX12).
27. Product catalog of Osram Opto-Semiconductors LED.
28. H. Kogelnik, Coupled wave theory for thick hologram gratings, *The Bell System Technical Journal*, 48, pp. 2909–2947 (1969).
29. H. Kogelnik and C.V. Shank, Coupled-wave theory of distributed feedback lasers, *Journal of Applied Physics*, 43, pp. 2327–2335 (1972).
30. A. Yariv, Coupled-mode theory for guided-wave optics, *IEEE Journal of Quantum Electronics*, 9, pp. 919–933 (1973).
31. D.G. Zill, *Advanced Engineering Mathematics*, PWS-KENT Publishing Co., Boston, 1992.
32. M. Ozisik, *Heat Conduction*, John Wiley and Sons, New York, 1980.
33. S. Moaveni, *Finite Element Analysis-theory and Application with ANSYS*, Prentice Hall, NJ, 2002.
34. R. Steenkiste and G. Springer, *Strain and Temperature Measurement with Fiber Optic Sensors*, Technomic Publishing Company, Lancaster, PA, 1997.

35. M. Weber, CRC Handbook of Laser Science and Technology Supplement 2: Optical Materials, CRC Press, Boca Raton, FL, 1995.
36. M. Yamada and K. Sakuda, Analysis of almost-periodic distributed slab waveguides via a fundamental matrix approach, *Applied Optics*, 26, pp. 3474–3478 (1987).
37. J.E. Sipe, L. Poladian, and C.M.D. Sterke, Propagation through non-uniform grating structures, *Journal of the Optical Society of America A*, 11, pp. 1307–1320 (1994).
38. L.A. Weller-Brophy and D.G. Hall, Analysis of waveguide gratings: application of Rouard's method, *Journal of the Optical Society of America A*, 2, pp. 863–871 (1985).
39. H.Y. Liu, G.D. Peng, and P.L. Chu, Thermal stability of gratings in PMMA and CYTOP polymer fibers, *Optics Communications*, 24, pp. 151–156 (2002).
40. G.D. Peng and P.L. Chu, Polymer optical fiber photosensitivities and highly tunable fiber gratings, *Fiber and Integrated Optics*, 19, pp. 277–293 (2000).
41. A. Kraus and A. Bar-Cohen, *Thermal Analysis and Control of Electronic Equipment*, Hemisphere Publishing Corp., New York, 1983.

APPENDIX 2.A. SOLUTION PROCEDURE TO OBTAIN THE OPTICAL POWER ALONG THE PFBG

Using $R(0) = 1$ and $S(L) = 0$, the following equation can be obtained from Equation (2.24)

$$r_1 + r_2 = 1, \quad (2A.1)$$

$$s_1 e^{mL} + s_2 e^{-mL} = 0. \quad (2A.2)$$

Substitution of the general solutions into the coupled-mode equation yields

$$\frac{dR}{dz} = \frac{d}{dz}(r_1 e^{mz} + r_2 e^{-mz}) = -\left(\frac{\hat{a}}{2} + i\delta\right)(r_1 e^{mz} + r_2 e^{-mz}) - i\kappa(s_1 e^{mz} + s_2 e^{-mz}). \quad (2A.3)$$

The above equation can be rearranged as

$$e^{mz} \left[r_1 \left(m + \frac{\hat{a}}{2} \right) + i(\delta r_1 + \kappa s_1) \right] + e^{-mz} \left[r_2 \left(-m + \frac{\hat{a}}{2} \right) + i(\delta r_2 + \kappa s_2) \right] = 0, \quad (2A.4)$$

which produces two additional conditions required to determine the four constants in the general solution as

$$r_1 \left(m + \frac{\hat{a}}{2} \right) = -i(\delta r_1 + \kappa s_1), \quad (2A.5)$$

$$r_2 \left(-m + \frac{\hat{a}}{2} \right) = -i(\delta r_2 + \kappa s_2). \quad (2A.6)$$

Solving four simultaneous equations [(2A.1), (2A.2), (2A.5), and (2A.6)], the coefficients of the general solution can be obtained as

$$r_1 = \frac{m - \left(\frac{\hat{a}}{2} + i\delta\right)}{m - \left(\frac{\hat{a}}{2} + i\delta\right) + \left[m + \left(\frac{\hat{a}}{2} + i\delta\right)\right]e^{2mL}}, \quad (2A.7)$$

$$r_2 = \frac{\left[m + \left(\frac{\hat{a}}{2} + i\delta\right)\right]e^{2mL}}{m - \left(\frac{\hat{a}}{2} + i\delta\right) + \left[m + \left(\frac{\hat{a}}{2} + i\delta\right)\right]e^{2mL}}, \quad (2A.8)$$

$$s_1 = \frac{m^2 - \left(\frac{\hat{a}}{2} + i\delta\right)^2}{-i\kappa \left\{m - \left(\frac{\hat{a}}{2} + i\delta\right) + \left[m + \left(\frac{\hat{a}}{2} + i\delta\right)\right]e^{2mL}\right\}}, \quad (2A.9)$$

$$s_2 = \frac{\left[m^2 - \left(\frac{\hat{a}}{2} + i\delta\right)^2\right]e^{2mL}}{i\kappa \left\{m - \left(\frac{\hat{a}}{2} + i\delta\right) + \left[m + \left(\frac{\hat{a}}{2} + i\delta\right)\right]e^{2mL}\right\}}. \quad (2A.10)$$

Coefficients for the solution of axial powers are

$$c_1 = \left(m_1 - \frac{\hat{a}}{2}\right)^2 + (m_2 - \delta)^2, \quad (2A.11)$$

$$c_2 = \left(m_1 + \frac{\hat{a}}{2}\right)^2 + (m_2 + \delta)^2, \quad (2A.12)$$

$$c_3 = 2e^{2m_1L} \left[m_1^2 + m_2^2 - \left(\frac{\hat{a}}{2}\right)^2 - \delta^2 \right], \quad (2A.13)$$

$$c_4 = -4e^{2m_1L} \left(-m_1\delta + m_2\frac{\hat{a}}{2} \right), \quad (2A.14)$$

$$c_5 = 2e^{2m_1L} \left\{ \left[m_1^2 + m_2^2 - \left(\frac{\hat{a}}{2}\right)^2 - \delta^2 \right] \cos(2m_2L) + 2 \left(-m_1\delta + m_2\frac{\hat{a}}{2} \right) \sin(2m_2L) \right\}, \quad (2A.15)$$

$$c_6 = \left[m_1^2 - m_2^2 - \left(\frac{\hat{a}}{2}\right)^2 + \delta^2 \right]^2 + 4 \left(m_1m_2 - \frac{\hat{a}}{2}\delta \right)^2, \quad (2A.16)$$

$$\begin{aligned}
c_7 = 2\kappa^2 e^{2m_1 L} & \left\{ \left[m_1^2 + m_2^2 - \left(\frac{\hat{a}}{2} \right)^2 - \delta^2 \right] \cos(2m_2 L) \right. \\
& \left. + 2 \cdot \left(-m_1 \delta + m_2 \frac{\hat{a}}{2} \right) \sin(2m_2 L) \right\}.
\end{aligned} \tag{2A.17}$$

APPENDIX 2.B. SOLUTION PROCEDURE TO DETERMINE THE TEMPERATURE PROFILE ALONG THE PFBG

2.B.1. Solution Procedure of the Temperature Profile Along the PFBG with the LED

Substituting the proposed particular solution into the conduction equation [Equation (2.47)], the coefficient of the particular solution can be obtained as

$$D = \frac{P_{inc} \hat{a}}{(p^2 - \hat{a}^2)(\pi r_o^2 k)}. \tag{2B.1}$$

Using boundary conditions, both ends of Bragg grating are adiabatic,

$$\left. \frac{d\theta}{dz} \right|_{z=0} = pg_1 - pg_2 - \hat{a}D = 0, \tag{2B.2}$$

$$\left. \frac{d\theta}{dz} \right|_{z=L} = pg_1 e^{pL} - pg_2 e^{-pL} - \hat{a}D e^{-\hat{a}L} = 0. \tag{2B.3}$$

Two coefficients of the general solution can be determined as

$$g_1 = \frac{\hat{a}D(e^{-\hat{a}L} - e^{-pL})}{p(e^{pL} - e^{-pL})}, \tag{2B.4}$$

$$g_2 = g_1 - \frac{\hat{a}}{p}D. \tag{2B.5}$$

2.B.2. Solution Procedure of the Temperature Profile Along the PFBG with the SM LD

Rearranging the non-homogeneous term in the conduction equation associated with the SM LD [Equation (2.52)] yields

$$\begin{aligned}
\left[-\frac{G(z)}{k} \right] &= \frac{-P_{inc}}{k\pi r_o^2} \cdot \hat{a} \int_{\lambda_1}^{\lambda_4} \overline{P(\lambda)} \left[(|R(\lambda, z)|)^2 + (|S(\lambda, z)|)^2 \right] d\lambda \\
&= \frac{-P_{inc}}{k\pi r_o^2} \cdot \hat{a} \int_{\lambda_1}^{\lambda_4} B e^{4 \ln 0.5 \left(\frac{\lambda - \lambda_c}{FWHM} \right)^2} \cdot [a_1(\lambda) e^{2m_1(\lambda)z} + a_2(\lambda) e^{2m_1(\lambda)(2L-z)}] d\lambda \\
&\quad - \frac{P_{inc}}{k\pi r_o^2} \cdot \hat{a} \int_{\lambda_2}^{\lambda_3} B e^{4 \ln 0.5 \left(\frac{\lambda - \lambda_c}{FWHM} \right)^2} \cdot (a_3(\lambda) \cos(2m_2(\lambda)(z - L)) \\
&\quad + a_4(\lambda) \sin(2m_2(\lambda)(z - L))) d\lambda
\end{aligned}$$

$$\begin{aligned}
& - \frac{P_{inc}}{k\pi r_o^2} \cdot \hat{a} \int_{\lambda_1}^{\lambda_2} B e^{4 \ln 0.5 \left(\frac{\lambda - \lambda_c}{FWHM} \right)^2} \\
& \quad \times \left\{ a_3(\lambda) \left[\left(\frac{1 - \cos(2m_2(\lambda)L)}{L} \right) z + \cos[2m_2(\lambda)L] \right] \right. \\
& \quad \left. + a_4(\lambda) \left(\frac{\sin(2m_2(\lambda)L)}{L} z - \sin[2m_2(\lambda)L] \right) \right\} d\lambda \\
& - \frac{P_{inc}}{k\pi r_o^2} \cdot \hat{a} \int_{\lambda_3}^{\lambda_4} B e^{4 \ln 0.5 \left(\frac{\lambda - \lambda_c}{FWHM} \right)^2} \\
& \quad \times \left\{ a_3(\lambda) \left(\left[\frac{1 - \cos(2m_2(\lambda)L)}{L} \right] z + \cos[2m_2(\lambda)L] \right) \right. \\
& \quad \left. + a_4(\lambda) \left(\frac{\sin[2m_2(\lambda)L]}{L} z - \sin[2m_2(\lambda)L] \right) \right\} d\lambda, \quad (2B.6)
\end{aligned}$$

$$\begin{aligned}
a_1(\lambda) &= \frac{c_1}{c_1 + c_5 + c_2 e^{4m_1 L}} + \frac{c_6}{\kappa^2 c_2 e^{4m_1 L} + 2\kappa^2 c_5 + \kappa^2 c_1}, \\
a_2(\lambda) &= \frac{c_2}{c_1 + c_5 + c_2 e^{4m_1 L}} + \frac{c_6}{\kappa^2 c_2 e^{4m_1 L} + 2\kappa^2 c_5 + \kappa^2 c_1}, \\
a_3(\lambda) &= \frac{c_3}{c_1 + c_5 + c_2 e^{4m_1 L}} + \frac{c_6}{\kappa^2 c_2 e^{4m_1 L} + 2\kappa^2 c_5 + \kappa^2 c_1} (-2e^{2m_1 L}), \\
a_4(\lambda) &= \frac{c_4}{c_1 + c_5 + c_2 e^{4m_1 L}}.
\end{aligned}$$

The particular solution can take a form as

$$\begin{aligned}
\theta_p &= \int_{\lambda_1}^{\lambda_4} F(\lambda) e^{2m_1(\lambda)z} d\lambda + \int_{\lambda_1}^{\lambda_4} G(\lambda) e^{-2m_1(\lambda)z} d\lambda + \int_{\lambda_2}^{\lambda_3} H(\lambda) \cos[M(\lambda)(z - L)] d\lambda \\
&+ \int_{\lambda_2}^{\lambda_3} N(\lambda) \sin[U(\lambda)(z - L)] d\lambda + \int_{\lambda_1}^{\lambda_2} V(\lambda) z + W(\lambda) d\lambda \\
&+ \int_{\lambda_3}^{\lambda_4} V(\lambda) z + W(\lambda) d\lambda + \int_{\lambda_1}^{\lambda_2} X(\lambda) z + Y(\lambda) d\lambda \\
&+ \int_{\lambda_3}^{\lambda_4} X(\lambda) z + Y(\lambda) d\lambda. \quad (2B.7)
\end{aligned}$$

By substituting the above particular solution [Equation (2B.7)] into the governing equation (Equation (2.52)), one can obtain the following equation.

$$\begin{aligned}
& \int_{\lambda_1}^{\lambda_4} \{4[m_1(\lambda)]^2 - p^2\} F(\lambda) e^{2m_1(\lambda)z} d\lambda + \int_{\lambda_1}^{\lambda_4} \{4[m_1(\lambda)]^2 - p^2\} G(\lambda) e^{-2m_1(\lambda)z} d\lambda \\
& - \int_{\lambda_2}^{\lambda_3} \{[M(\lambda)]^2 + p^2\} H(\lambda) \cos[M(\lambda)(z - L)] d\lambda
\end{aligned}$$

$$\begin{aligned}
& - \int_{\lambda_2}^{\lambda_3} \{ [U(\lambda)]^2 + p^2 \} N(\lambda) \sin[U(\lambda)(z - L)] d\lambda \\
& - p^2 \int_{\lambda_1}^{\lambda_2} V(\lambda)z + W(\lambda) + X(\lambda)z + Y(\lambda) d\lambda \\
& - p^2 \int_{\lambda_3}^{\lambda_4} V(\lambda)z + W(\lambda) + X(\lambda)z + Y(\lambda) d\lambda \\
& = \frac{-P_{inc}}{k\pi r_o^2} \cdot \hat{a} \int_{\lambda_1}^{\lambda_4} B e^{4 \ln 0.5 \left(\frac{\lambda - \lambda_c}{FWHM} \right)^2} \cdot [a_1(\lambda) e^{2m_1(\lambda)z} + a_2(\lambda) e^{2m_1(\lambda)(2L-z)}] d\lambda \\
& - \frac{P_{inc}}{k\pi r_o^2} \cdot \hat{a} \int_{\lambda_2}^{\lambda_3} B e^{4 \ln 0.5 \left(\frac{\lambda - \lambda_c}{FWHM} \right)^2} \cdot \{ a_3(\lambda) \cos[2m_2(\lambda)(z - L)] \\
& \quad + a_4(\lambda) \sin[2m_2(\lambda)(z - L)] \} d\lambda \\
& - \frac{P_{inc}}{k\pi r_o^2} \cdot \hat{a} \int_{\lambda_1}^{\lambda_2} B e^{4 \ln 0.5 \left(\frac{\lambda - \lambda_c}{FWHM} \right)^2} \\
& \quad \times \left\{ a_3(\lambda) \left(\left(\frac{1 - \cos[2m_2(\lambda)L]}{L} \right) z + \cos[2m_2(\lambda)L] \right) \right. \\
& \quad \left. + a_4(\lambda) \left(\frac{\sin[2m_2(\lambda)L]}{L} z - \sin[2m_2(\lambda)L] \right) \right\} d\lambda \\
& - \frac{P_{inc}}{k\pi r_o^2} \cdot \hat{a} \int_{\lambda_3}^{\lambda_4} B e^{4 \ln 0.5 \left(\frac{\lambda - \lambda_c}{FWHM} \right)^2} \\
& \quad \times \left\{ a_3(\lambda) \left(\left(\frac{1 - \cos[2m_2(\lambda)L]}{L} \right) z + \cos[2m_2(\lambda)L] \right) \right. \\
& \quad \left. + a_4(\lambda) \left(\frac{\sin[2m_2(\lambda)L]}{L} z - \sin[2m_2(\lambda)L] \right) \right\} d\lambda. \tag{2B.8}
\end{aligned}$$

The spectrally dependent coefficients of the particular solution can be found by comparing coefficients in each term of Equation (2B.8) as

$$F(\lambda) = \frac{\frac{-P_{inc}}{k\pi r_o^2} \cdot \hat{a} \cdot B e^{4 \ln 0.5 \left(\frac{\lambda - \lambda_c}{FWHM} \right)^2} \cdot a_1(\lambda)}{4[m_1(\lambda)]^2 - p^2}, \tag{2B.9}$$

$$G(\lambda) = \frac{\frac{-P_{inc}}{k\pi r_o^2} \cdot \hat{a} \cdot B e^{4 \ln 0.5 \left(\frac{\lambda - \lambda_c}{FWHM} \right)^2} \cdot a_2(\lambda) \cdot e^{4L \cdot m_1(\lambda)}}{4[m_1(\lambda)]^2 - p^2}, \tag{2B.10}$$

$$M(\lambda) = U(\lambda) = 2m_2(\lambda), \tag{2B.11}$$

$$H(\lambda) = \frac{\frac{P_{inc}}{k\pi r_o^2} \cdot \hat{a} \cdot B e^{4 \ln 0.5 \left(\frac{\lambda - \lambda_c}{FWHM} \right)^2} \cdot a_3(\lambda)}{4[m_2(\lambda)]^2 + p^2}, \quad (2B.12)$$

$$N(\lambda) = \frac{\frac{P_{inc}}{k\pi r_o^2} \cdot \hat{a} \cdot B e^{4 \ln 0.5 \left(\frac{\lambda - \lambda_c}{FWHM} \right)^2} \cdot a_4(\lambda)}{4[m_2(\lambda)]^2 + p^2}, \quad (2B.13)$$

$$V(\lambda) = \frac{\frac{P_{inc}}{k\pi r_o^2} \cdot \hat{a} \cdot B e^{4 \ln 0.5 \left(\frac{\lambda - \lambda_c}{FWHM} \right)^2} \cdot a_3(\lambda)}{p^2} \frac{[1 - \cos(2m_2L)]}{L}, \quad (2B.14)$$

$$W(\lambda) = \frac{\frac{P_{inc}}{k\pi r_o^2} \cdot \hat{a} \cdot B e^{4 \ln 0.5 \left(\frac{\lambda - \lambda_c}{FWHM} \right)^2} \cdot a_3(\lambda)}{p^2} \cos(2m_2L), \quad (2B.15)$$

$$X(\lambda) = \frac{\frac{P_{inc}}{k\pi r_o^2} \cdot \hat{a} \cdot B e^{4 \ln 0.5 \left(\frac{\lambda - \lambda_c}{FWHM} \right)^2} \cdot a_4(\lambda)}{p^2} \frac{\sin(2m_2L)}{L}, \quad (2B.16)$$

$$Y(\lambda) = \frac{-\frac{P_{inc}}{k\pi r_o^2} \cdot \hat{a} \cdot B e^{4 \ln 0.5 \left(\frac{\lambda - \lambda_c}{FWHM} \right)^2} \cdot a_4(\lambda)}{p^2} \sin(2m_2L). \quad (2B.17)$$

Assuming that all the heat loss occurs from the surface of the fiber and neglecting the axial conduction at the fiber ends, i.e., assuming that both ends of the BGs are adiabatic, the following two boundary conditions can be obtained

$$\left. \frac{d\theta}{dz} \right|_{z=0} = 0 \quad \text{and} \quad \left. \frac{d\theta}{dz} \right|_{z=L} = 0.$$

Applying the above BCs to the general solution for the excess temperature [Equation (2.53)],

$$\begin{aligned} \theta'(0) = & pd_1 - pd_2 + \int_{\lambda_1}^{\lambda_4} 2m_1(\lambda)[F(\lambda) - G(\lambda)]d\lambda \\ & + \int_{\lambda_2}^{\lambda_3} H(\lambda)M(\lambda)\sin[L \cdot M(\lambda)]d\lambda + \int_{\lambda_2}^{\lambda_3} N(\lambda)M(\lambda)\cos[L \cdot M(\lambda)]d\lambda \\ & + \int_{\lambda_1}^{\lambda_2} V(\lambda) + X(\lambda)d\lambda + \int_{\lambda_3}^{\lambda_4} V(\lambda) + X(\lambda)d\lambda = 0, \end{aligned} \quad (2B.18)$$

$$\begin{aligned} \theta'(L) = & pd_1 e^{pL} - pd_2 e^{-pL} + \int_{\lambda_1}^{\lambda_4} 2m_1(\lambda)F(\lambda)e^{2m_1(\lambda)L}d\lambda \\ & - \int_{\lambda_1}^{\lambda_4} 2m_1(\lambda)G(\lambda)e^{-2m_1(\lambda)L}d\lambda + \int_{\lambda_2}^{\lambda_3} N(\lambda)M(\lambda)d\lambda \\ & + \int_{\lambda_1}^{\lambda_2} V(\lambda) + X(\lambda)d\lambda + \int_{\lambda_3}^{\lambda_4} V(\lambda) + X(\lambda)d\lambda = 0. \end{aligned} \quad (2B.19)$$

Solving (2B.14) and (2B.15) simultaneously, the two coefficients of the general solution can be determined as

$$\begin{aligned}
 d_1 = \frac{1}{p(1 - e^{2pL})} & \left\{ \int_{\lambda_1}^{\lambda_4} -2m_1(\lambda) [F(\lambda)(1 - e^{L[2m_1(\lambda)+p]}) \right. \\
 & \quad \left. - G(\lambda)(1 - e^{-L[2m_1(\lambda)-p]})] d\lambda \right. \\
 & \quad - \int_{\lambda_2}^{\lambda_3} H(\lambda)M(\lambda) \sin[L \cdot M(\lambda)] + N(\lambda)M(\lambda) (\cos[L \cdot M(\lambda)] - e^{pL}) d\lambda \\
 & \quad \left. - \int_{\lambda_1}^{\lambda_2} [V(\lambda) + X(\lambda)](1 - e^{pL}) d\lambda - \int_{\lambda_3}^{\lambda_4} [V(\lambda) + X(\lambda)](1 - e^{pL}) d\lambda \right\},
 \end{aligned} \tag{2B.20}$$

$$\begin{aligned}
 d_2 = d_1 + \frac{1}{p} & \left\{ \int_{\lambda_1}^{\lambda_4} 2m_1(\lambda) [F(\lambda) - G(\lambda)] d\lambda \right. \\
 & \quad + \int_{\lambda_2}^{\lambda_3} H(\lambda)M(\lambda) \sin[L \cdot M(\lambda)] + N(\lambda)M(\lambda) \cos[L \cdot M(\lambda)] d\lambda \\
 & \quad \left. + \int_{\lambda_1}^{\lambda_2} V(\lambda) + X(\lambda) d\lambda + \int_{\lambda_3}^{\lambda_4} V(\lambda) + X(\lambda) d\lambda \right\}.
 \end{aligned} \tag{2B.21}$$

Micro- and Opto-Electronic Materials and Structures:
Physics, Mechanics, Design, Reliability, Packaging
Volume I Materials Physics - Materials Mechanics.
Volume II Physical Design - Reliability and Packaging
Suhir, E.; Lee, Y.C.; Wong, C.P. (Eds.)
2007, LXII, 1460 p. In 2 volumes, not available
separately., Hardcover
ISBN: 978-0-387-27974-9